Master's thesis

NTNU
Norwegian University of Science and Technology
Faculty of Natural Sciences
Department of Chemical Engineering

Veslemøy Selvik

Microfluidic Interfacial Tension

Model development and testing.

Master's thesis in Chemical Engineering
Supervisor: Gisle Øye
Co-supervisor: Marcin Dudek and Jens Norrman
June 2022

NTNU
Norwegian University of
Science and Technology

Veslemøy Selvik

Microfluidic Interfacial Tension

Model development and testing.

Master's thesis in Chemical Engineering
Supervisor: Gisle Øye
Co-supervisor: Marcin Dudek and Jens Norrman
June 2022

Norwegian University of Science and Technology
Faculty of Natural Sciences
Department of Chemical Engineering

NTNU
Norwegian University of
Science and Technology

Abstract

A method for interfacial tension measurements using microfluidic technology has been developed. The development follow methodology published in literature. A non-ionic surfactant was employed to manipulate the interfacial tension and the deformation of droplets was used to determine the IFT.

The experimental setup included specially designed chips with a series of expansions and constrictions. Syringe pumps were used to manipulate the flow in the chip, and an inverted microscope was used to observe the chip. A high-speed camera was used to capture the flow and recordings were analysed by a neural network. A model was fitted to the systems by using measurements from a ring tensiometer as reference. The validity of the model was examined, and a sensitivity analysis was made. Dynamic and static IFT measurements was achieved with good accuracy. Some phenomena related to droplet relaxation was observed, but not explored further due to time constraints.

The developed measurement technique offers several advantages. The sample size is reduced tenfold in comparison to the ring tensiometer. The measurement time was reduced from days to hours. The possibilities of using the setup for several applications makes the microfluidic tensiometry a promising technology in future labs. However, some weaknesses are identified. No universal model has been developed. This means that for any oil/surfactant system the model must be developed. This development still requires a traditional tensiometer meaning the technology is not stand-alone yet.

Future work includes the exploration of different chip designs and chemical composition. Developing a new methodology of model development where deformation is related to the interfacial tension through natural laws would be a large improvement.

En metode for å måle overflatespenning ved hjelp av microfluidics har blitt utviklet. Utviklingen av modellen følger metodikk publisert i litteraturen. En ikke-ionisk surfaktant ble brukt for å manipulere overflatespenning og deformasjon av dråper ble brukt for å fastslå grenseflatespenningen.

Det eksperimentelle oppsettet inkluderer spesiallagde chips med en serie ekspansjoner og innsnevringer. En pumpe ble brukt for å kontrollere strømmingen i chipen og et invertert mikroskop ble brukt for å observere chippen. Et høyhastighets kamera ble brukt for for å ta bilder av strømningen og et nevralt nettverk ble brukt for å analysere bildene i etterkant. Parametere i modellen ble bestemt ved å tilpasse resultatene til målinger gjort med et ring tensiometer. Validering av modellen er diskutert og en sensitivitets analyse er gjennomført. Både dynamiske og statiske målinger er presentert, med god nøyaktighet. Fenomener relatert til dråpe relaksjon er observert, men ikke diskutert videre grunnet tidsbegrensinger.

Den utviklede metoden har flere fordeler. Prøve størrelsen er redusert med en faktor av ti i forhold til ring tensiometeret. Tiden per måling er redusert fra dager til timer. Muligheten for å bruke det samme instrumentet til flere typer målinger gjør microfluidics til en lovende teknologi i fremtidens labber. Når det er sagt så ble flere svakheter ved metoden identifisert. Modellen utviklet er ikke universal. Det betyr at for hvert olje/surfaktant system må modellens parametere fastslåes på nytt. På dette stadiet er modellen fortsatt avhengig av et tradisjonelt tensiometer, og kan derfor ikke brukes frittstående.

Fremtidig arbeid inkluderer utforskingen av nye chip design og kjemiske systemer. Å utvikle en modell som relaterer deformasjon til overflatespenning gjennom naturlover vil være en stor forbedring.

I would like to express my gratitude to my supervisor Gisle Øye for presenting me with this project. His door was always open and I am grateful for his guidance throughout the past year. I would also like to express my gratitude to my co-supervisors. To Jens; for all the hours he has spent discussing a large variety of topics with me. To Marcin; for his advice in both academic and personal matters over the past year. I want to thank all members of Ugelstad Laboratory for the extraordinary learning environment you provide. Finally, I want to thank Amund for his continuous support through everything.

Thank you.

Contents

List of Figures

List of Tables

List of symbols

List of symbols and their description.

Symbol	**Description**
A	Area
$\mathbf{a}$	Local acceleration
a	Activity
α	Effective viscosity
a_0	Equilibrium radius
b	Buoyancy
D	Deformation
δ	Deformation
η	Viscosity
$\hat{\eta}$	Viscosity ratio
$\dot{\epsilon}$	Extension rate
F	Helmholtz free energy
$\hat{\mathbf{F}}$	Local body force
F	Force
f	Correction factor
γ	Interfacial tension
Γ	Surface excess
G	Gibbs free energy
H	Height
μ	Chemical potential
$\mathbf{M}$	Local force
n	Number of moles
$\mathbf{n}$	Local force
P or p	Pressure
ρ	Density
R	Gas constant
R	Radius
S	Entropy
s	Surface
σ	Interfacial tension
s	Distance
T	Temperature
t	Time
U	Internal energy
U	Velocity
V	Volume
W	Width
$\mathrm{w_r}$	Weight of ring

Chapter 1

Introduction

This thesis is written as the final project of the master program in chemical engineering at the Norwegian University of Science and Technology, NTNU. The work reported in this document was carried out at Ugelstad Laboratories in the spring of 2022. The objective of this master thesis was to develop a methodology of interfacial tension measurements using microfluidic methods.

A colloidal system is any system where one phase is dispersed in another. Examples are emulsions, aerosols, and suspensions. A natural consequence of this is the formation of interfaces in the intersection between the two phases. These systems are found in nature but are also utilized in industrial production and products. Applications range from paint and petroleum to paper and food. Since the interfacial area in colloidal systems is very large it is crucial to understand phenomena occurring at the interface, and how to manipulate the interface.

Interfacial tension (IFT) is a measure of the force of attraction between molecules at the interface. This force acts to reduce the interfacial area and is essential in understanding emulsion formation and stability. The IFT of a system can be manipulated by the addition of surface-active agents. These molecules adsorb at the interface, altering the surface free energy.[1]

Several methods of measuring IFT are established. These offer a wide range of measurements spanning several time domains. Static measurements for a range of concentrations can give information about the surfactant aggregates called micelles. Dynamic measurements over a period of time offer insight into the kinetics of surfactant adsorption to the interface. Traditional tensiometers are often bulky and require large sample sizes.[2]

With the emergence of new technology, other measurement techniques have been proposed. Microfluidics is a rapidly expanding technology dealing with manipulations of flow on a micrometer scale. This is achieved by specially manufactured chips in combination with a microscope and syringe pumps. Advantages of microfluidic tensiometry include a reduction in sample size and instrument footprint. The time required for each measurement is also reduced and the microfluidic set-up can potentially replace several instruments in a common lab.[3]

In this report, a method first proposed by Brosseau et al. will be explored, replicated, and improved.[4] A model giving the relationship between droplet deformation and interfacial tension will be developed using measurements from a ring tensiometer as a reference. The model will then be examined to determine the validity of the methodology used.

Chapter 2

Background

This chapter offers background on interfacial phenomena such as interfacial tension, emulsion formation, and surfactants. Interfacial tension measurements with standard instrumentation and microfluidics will be presented.

2.1 Interfacial tension

When two phases are in contact, an interface is formed between them. A contractive force acts to minimize the contact area, this force is quantified by the interfacial tension (IFT). Work is required to expand the interfacial area and the energy required per unit area is numerically equal to the interfacial tension. The IFT is commonly given with the units mN/m.[1]

The interfacial tension is caused by unbalanced forces acting on the molecules at the interface.[5] Molecules in the bulk have uniform interactions with each other in all directions, while at the interface interactions with molecules of both phases occur. The forces between molecules of the same phase are stronger than that of the continuous phase which results in a net force towards the bulk. Figure 2.1.1 offers a visual representation of this phenomenon. The net interaction forces are shown for a selection of molecules. The result is a tendency to form the shape of minimum surface area. The geometry with the smallest surface area is two completely separated phases. However, the surface-to-volume ratio of spheres is small and droplets will therefore form and coalesce until the phase separation is complete. This mechanism is essential for the formation of emulsions, where one phase is dispersed as small droplets in the other.[6]

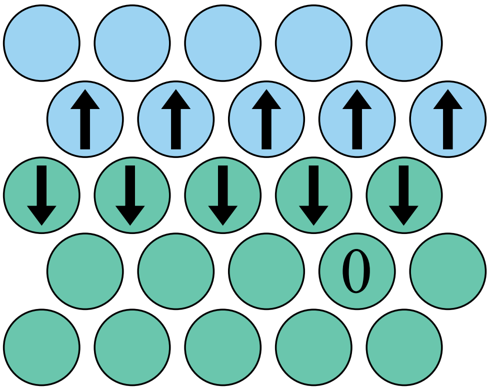

Figure 2.1.1: Molecules at the interface experience different forces than molecules in the bulk. The net interaction forces are shown inside selected molecules. Figure inspired by Myers.[7]

The interfacial tension can be described using a thermodynamic or mechanical approach. Both derivations will be described briefly in the following paragraphs.[8]

2.1.1 Thermodynamic approach

It is useful to describe the interface as a mathematical surface with zero thickness because the differential geometries are well understood. In reality, however, the interface is a three-dimensional phenomenon. Gibbs introduced a reference surface, s, in the interfacial region. An interfacial region between bulk fluid A and B includes this surface and the surface is perpendicular to density and concentration gradients. The surfaces of bulk A, s_A, and B, s_B, are parallel to s. Figure 2.1.2 show this. s must be included for any property in the interfacial region surrounding. In this region the composition and properties vary, while constant in the bulk. Surface excess quantities are therefore used.[8] Equation 2.1.1 show the surface excess of component i between two bulk phases, A and B.

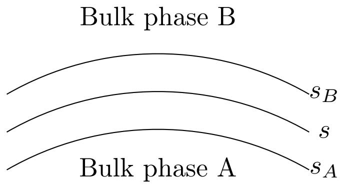

Figure 2.1.2: Nomenclature use in Section 2.1.1

$$n_i^s = n_i - n_{iA} - n_{iB} \tag{2.1.1}$$

Where n_i is the number of moles i in the region between s_A and s_B. n_{iX} represents the number of moles of i if the region between s_X and s was occupied by bulk phase X alone. Where X is A or B.

At equilibrium and constant shape of the surface, the internal energy can be assumed to be a function of entropy, S, and the number of moles of species i, n_i. From thermodynamics we have:

$$dU = TdS + \sum_i \mu_i \, dn_i \tag{2.1.2}$$

where

$$T = \left(\frac{\partial U}{\partial S}\right)_{n_i,\text{shape}} \qquad \mu_i = \left(\frac{\partial U}{\partial n_i}\right)_{n_j,S,\text{shape}}$$

Bulk phase A is now considered unchanged while some mass or energy is transferred to bulk phase B and the interfacial region. An energy balance can be constructed using the first law of thermodynamics.

$$dU_{tot} = 0 = T\,dS + \sum_i \mu_i \, dn_i + T_B \, dS_B + \sum_i \mu_{iB} \, dn_{iB} \tag{2.1.3}$$

The mass balance for various species must be $dn_i = -dn_{iB}$ And the entropy of a system in equilibrium is at its maximum according to the second law of thermodynamics such that $dS_{tot} = 0 = dS + dS_B$. Equation 2.1.3 can therefore be written as shown in Equation 2.1.4.

$$0 = (T - T_B)dS + \sum_i (\mu_i - \mu_{iB}) \, dn_i \tag{2.1.4}$$

It is clear that $T = T_B$ and $\mu_i = \mu_{iB}$ to ensure Equation 2.1.4 holds for all possible changes. Using the same procedure a similar conclusion can be reached when considering mass and energy transfer between bulk A and the interface. Equation 2.1.2 can therefore be written as shown in Equation 2.1.5.

$$dU^s(\text{Fixed shape}) = T\,dS^s + \sum_i \mu_i \, dn_i^s \tag{2.1.5}$$

Up until this point the shape of the surface has been assumed constant. Deformation of the surface will change both the area and curvature. To account for this, a new term is included.

$$dU^s = T\,dS^s + \sum_i \mu_i \, dn_i^s + \gamma \, dA \tag{2.1.6}$$

where γ is the interfacial tension defined as $(\partial U^s/\partial A)_{S^s,n_i^s}$. Substituting the internal free energy by the Helmholtz free energy ($F = U - TS$) we get

$$dF^s = -S^s \, dT + \sum_i \mu_i \, dn_i^s + \gamma \, dA \tag{2.1.7}$$

The interfacial tension can be written in terms of surface excess free energy produced by an increase in area as shown in Equation 2.1.8.[8]

$$\gamma = \left(\frac{\partial F^s}{\partial A}\right)_{T,n_i^s} \tag{2.1.8}$$

2.1.2 Mechanical approach

Interfacial tension at a static equilibrium can also be defined by a mechanical approach. A three-dimensional system is considered to include a lateral boundary condition, s_o. Figure 2.1.3 show the system. Within this region tangential pressures, p_T, and normal pressures, p_N, varies. The pressures in the bulk is isotropic and $p_T = p_N$.[8] Newton's second law can then be applied to the interfacial region as shown in Equation 2.1.9. $\hat{\mathbf{F}}$ is the local body force, most commonly gravity, and $\mathbf{a}$ is the local acceleration. $\mathbf{n}$ and $\mathbf{M}$ are the local forces as shown in Figure 2.1.3.

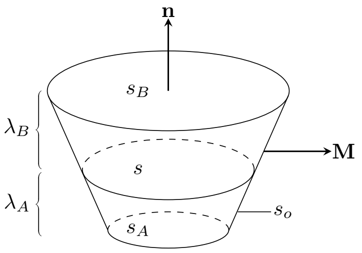

Figure 2.1.3: Nomenclature used in Section 2.1.2

$$\int_V \rho\hat{\mathbf{F}}\,dV + \int_{s_A} p_A\mathbf{n}\,dS - \int_{s_B} p_B\mathbf{n}\,dS - \int_{s_o} p_T\mathbf{M}\,ds = \int_V \rho\mathbf{a}\,dV \tag{2.1.9}$$

Using surface excess as described earlier one can describe the case of the region between s_A and s being occupied by bulk phase A as

$$\int_{V_A} \rho_A\hat{\mathbf{F}}\,dV + \int_{s_A} p_A\mathbf{n}\,dS - \int_{s} p_A\mathbf{n}\,dS - \int_{s_{oA}} p_A\mathbf{M}\,ds = \int_{V_A} \rho_A\mathbf{a}\,dV \tag{2.1.10}$$

And similarly for bulk phase B occupying the region between surface s_B and s:

$$\int_{V_B} \rho_B\hat{\mathbf{F}}\,dV + \int_{s_B} p_B\mathbf{n}\,dS - \int_{s} p_B\mathbf{n}\,dS - \int_{s_{oB}} p_B\mathbf{M}\,ds = \int_{V_B} \rho_B\mathbf{a}\,dV \tag{2.1.11}$$

Subtracting Equation 2.1.10 and 2.1.11 from Equation 2.1.9 we get:

$$\int_V \Delta\rho\hat{\mathbf{F}}\,dV + \int_s (p_A - p_B)\mathbf{n}\,dS - \int_{s_o} p_T\mathbf{M}\,ds = \int_V \Delta\rho\mathbf{a}\,dV \tag{2.1.12}$$

By assuming the interfacial thickness is small compared to the radius of curvature and uniform body forces between s_A and s_B. And applying Weatherburns theorem from differential geometry,[8] Equation 2.1.12 becomes:

$$\Gamma\hat{\mathbf{F}} - \Gamma\mathbf{a} + (p_A - p_B)\mathbf{n} + 2H\gamma\mathbf{n} + \nabla_s\gamma = 0 \tag{2.1.13}$$

where Γ is the surface excess, H is the height and $\nabla_s\gamma$ is the gradient of IFT. Assuming uniform interfacial tension and applying the Young-Laplace equation the interfacial tension can be expressed as a function of the tangential pressure difference over a length, λ.

$$\gamma = -\int_{\lambda_A}^{\lambda_B} \Delta p_T\,d\lambda \tag{2.1.14}$$

2.2 Emulsions

For simplicity's sake we consider that emulsions generally fall into one of two categories: oil-in-water or water-in-oil, where the latter liquid forms the continuous phase. Other more complex systems exist, such as double emulsions, but this will not be described in more detail here. When forming emulsions with pure liquids, an unstable system is formed which will quickly separate. The reason for this is that the interfacial tension is often relatively high for pure systems. This causes a significant driving force towards the reduction of interfacial area.[9] Separation is not desirable in many applications. Examples are cosmetics and food applications which are taking advantage of emulsification.

Work is required to form an emulsion and the energy used is stored in the system as potential energy. The system is therefore thermodynamically unstable and will phase separate to minimize the potential energy. There are several destabilizing mechanisms of emulsions.[7] Coalescence refers to two (or more) droplets merging into one. This forms a larger droplet and reduces the total surface area. Flocculation is the formation of droplet clusters, and creaming is the result of a density difference between the dispersed and continuous phases.[7]

2.2.1 Emulsion stabilization with emulsifiers

To improve the stability of emulsions an emulsifier can be added. Bancroft's rule states that the phase in which the emulsifier is more soluble will be the continuous phase. Langmuir and Harkins expanded on the theory by recognizing the emulsifiers forming an oriented monolayer at the interface. Harkins' oriented wedge theory suggests that the largest part of the emulsifier molecule will orient in the continuous phase. This theory is somewhat unrealistic and there are many exceptions. Winsor elaborated on the Bancroft theory by considering the ratio between cohesion energies between the hydrophilic and lipophilic parts of the emulsifier.[9] Emulsion stabilization can be achieved through several mechanisms. Four mechanisms will be described in the next paragraphs.

Inorganic electrolytes introduce ions to the system. The ions adsorb at the interface forming a weak electrical double layer around the droplet. This slows the coalescence and aggregation of droplets and increases stability. However, in comparison to other mechanisms, the effect is weak and often used in combination with other approaches.

Polymeric stabilizers adsorbing on the interface reduce the energetic driving force of coalescence by forming a mechanical barrier and/or lowering the interfacial tension. The polymeric nature allows each polymer to adsorb at many sites on the droplet which decreases the rate of desorption. Polymers can also affect the viscosity of the continuous phase which slows down phenomena such as creaming.

Solid particles adsorbing at the interface can form a rigid barrier and a stabilizing film at the interface. The particles must be much smaller than the dispersed droplets and must be wetted by both aqueous and organic liquids. Attractive particle-particle interactions strengthen the system.

Finally, surfactants adsorbed at the interface can produce electrical, steric, and mechanical barriers between droplets, thus reducing coalescence. More details on surfactants can be found in the next section.[7]

2.3 Surfactants

The term surfactant is a contraction of the term *surf*ace-*act*ive-*a*ge*nt*. It is a substance characterized by the ability to adsorb on interfaces and alter the interfacial free energy. Surfactants consist of both hydrophobic and hydrophilic groups. Because of this, the name amphiphiles is also used.[10]

2.3.1 Tween20

The surfactant used in this thesis is Polysorbate 20 also called Tween 20. It is a non-ionic surfactant, meaning it bears no charge. The main advantage of non-ionic surfactants is their versatility in usage. They are compatible with most other surfactants and are generally available free of electrolytes. In addition, they can be made resistant to hard water and organic solvents.[10] The chemical structure of Tween 20 can be found in Figure 2.3.1. Tween 20 is widely used as a detergent in many applications. DNA extraction, protein purification, and food applications to name a few. The ethylene oxide subunits are hydrophilic while the hydrocarbon chains are hydrophobic.[11]

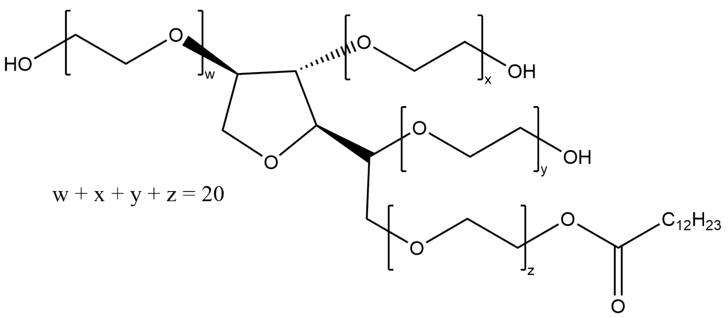

Figure 2.3.1: Molecular structure of Tween 20.

2.3.2 Adsorption

A key characteristic of surfactants is their hydrophobic and hydrophilic sections. When surfactants are dissolved in an aqueous solution there are unfavorable interactions between the hydrophobic groups and the water molecules. To reduce the unfavorable energetic interactions the surfactant adsorb on the interfaces, orienting the hydrophobic groups in a more favorable environment. At relatively low concentrations the surfactants will adsorb at the interface, while at higher concentrations aggregations, called micelles, form. When molecules exhibiting the amphiphilic nature of surfactants are dissolved in a solvent, the hydrophobic groups cause distortion of the solvent. This increases the overall free energy of the system and reduces the work required to transport the surfactant to the interface. This in turn decreases the work required to increase the interfacial area.[7]

The change of free energy in a system is described by Gibbs free energy as shown in Equation 2.3.1.

$$dG = -S\,dT + V\,dP + \gamma\,dA + \sum \mu_i\,dn_i \tag{2.3.1}$$

where S is entropy, T is temperature, V is volume, P is pressure, γ is the interfacial tension, A is the interfacial area, μ_i is the chemical potential of component i and n_i is the concentration of adsorbed material at the interface. By assuming temperature, pressure, and moles to be constant and the system to be in equilibrium one can reduce Equation 2.3.1 to $dG = \gamma\,dA$. Surface excess varies with adsorption yielding the Gibbs equation given in Equation 2.3.2. Gibbs equation relates the change of surface tension to the degree of adsorption and concentration in the bulk.

$$d\gamma_i = -\Gamma_1\,d\mu_1 - \Gamma_2\,d\mu_2 - \Gamma_3\,d\mu_3 - \cdots \tag{2.3.2}$$

γ_i is the interfacial tension of the solvent and Γ_i is the surface excess of component i. At equilibrium between the concentration in the bulk and at the interface, the chemical potential is defined in Equation 2.3.4 and the derivative is shown.

$$\mu_i = \mu_i^\circ + RT\ln(a_i) \tag{2.3.3}$$

$$d\mu_i = RT\,d\ln(a_i) \tag{2.3.4}$$

a_i is the activity of component i. Equation 2.3.2 can then be simplified as shown below.

$$d\gamma = -RT\sum_i \Gamma_i\,d\ln a_i \tag{2.3.5}$$

By assuming dilute solutions the activity is equal to the surfactant concentration. Further assuming a two-component system we get the relationship between surfactant concentration and interfacial tension as shown in Equation 2.3.6.[7]

$$\Gamma = -\frac{1}{RT}\frac{d\sigma}{d\ln C} \tag{2.3.6}$$

If the interfacial tension can be measured and the concentration is known one can determine the surface excess concentration of surfactant using this equation. This is a useful tool for the characterization of surfactants.[10]

2.3.3 Self-association

At high concentrations of surfactants self-association can be observed. Surfactants for aggregated when the interfaces are saturated. In an aqueous solution, surfactants arrange such that the hydrophobic segments are shielded from the bulk. These aggregations are called micelles and the concentration at which they occur is named the *c*ritical *m*icelle *c*oncentration or CMC.[10]

At the CMC distinct changes in the systems, properties can be seen. Interfacial tension, conductivity, and osmotic pressure are a few properties where this can be observed. Figure 2.3.2 show the change in IFT with increasing concentration of surfactant. CMC can be measured by this abrupt change in properties.

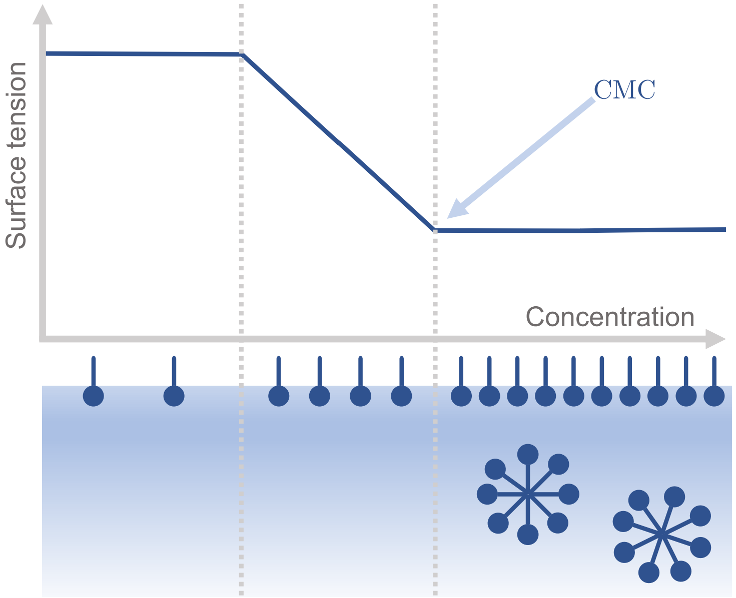

Figure 2.3.2: Illustration of surface tension as a function of surfactant concentration.

The entropy is expected to decrease when surfactants form micelles. However, the increase in entropy of the solvent is dominant. The water molecules arrange around the alkyl chains, so when the tails are shielded inside the micelles entropy is increased.

The shape of the micelles is dependent on the surfactant concentration. In dilute solutions, spherical micelles can be found. At higher concentrations, cylindrical and more complex structures are formed. Several factors influence the CMC; surfactant chain length, head group structure, and structure of the alkyl chain to name a few.[9]

2.4 Tensiometry

There are several established methods for interfacial tension measurements. The pendant drop, spinning drop, and Du Noüy ring are some examples. Each method has its advantages and disadvantages.

The pendant drop method relies on image analysis of the droplet curvature. A droplet is suspended from a capillary. The droplet has a higher density than the surrounding fluid. The gravitational pull on the droplet is opposed by the interfacial tension as the interfacial area is increased. This technique is suitable for liquid-gas and liquid-liquid systems. However, the continuous fluid must be transparent such that the droplet can be imaged. Since the droplet can be observed over time one can observe time-dependent phenomena. Low IFTs can be measured accurately.[8]

In the spinning drop tensiometer, the elongation of a droplet in a centrifugal field is used to determine the IFT. A drop of the denser fluid is placed in a horizontal tube, the tube is then rotated. The elongation due to the centrifugation causes an increase of the interfacial area which is opposed by the interfacial tension. An advantage of the spinning drop tensiometer is that very low IFTs can be measured and time-dependent phenomena can be observed. In addition, the method can be used in systems where the surrounding fluid has a small degree of turbidity.[8]

Capillary rise tensiometry includes a capillary partially inserted into a liquid. Attractive interactions between the liquid and the capillary cause the liquid to rise in the tube. Using the Young-Laplace equation the interfacial tension can be found from the density difference and the radius of curvature of the meniscus. This technique offers high accuracy but requires careful measurement by the user. The capillary must have a circular shape with known dimensions and must be placed vertically to avoid any errors.

Other tensiometers relate the interfacial tension to the vertical force acting on a solid body withdrawn from the liquid.[8] From this force, the IFT can be calculated based on the geometry of the object. The technique is named after the probe used. The Wilhelmy plate is a vertical sheet, while the Du Noüy ring is a horizontal ring. Later in this thesis, the ring tensiometer will be described in more detail. To avoid large errors in the measurement the probe must be void of any impurities and placed vertically (Wilhelmy plate) or horizontally (Du Noüy ring) in the liquid. Some advantages of this method are that the densities can be unknown and time effects can be observed.

2.5 Interfacial tension measurements with Microfluidic devices

Microfluidics is an emerging technology taking advantage of the manipulation of fluids on a micrometer scale. Costume-made chips in combination with a microscope and dosage system allows recording and control over phenomena inside the chip.[12;13] Measurements are fast and require small sample sizes. A large variation of chip designs allow the same instrument to be used for several applications which, in addition to the small footprint, makes a microfluidic setup desirable for any lab. The chips can be manufactured from a variety of materials. Glass, paper, and thermoset plastics to name a few.[14]

Several methods of tensiometry using microfluidic devices have been developed. Schroën et al. identified five different approaches to interfacial tension measurements; droplet size, pressure drop, droplet deformability, pH change related to adsorption kinetics, and the jetting/dripping transition.[15] In this thesis, only IFT measurements using droplet deformation will be discussed.

Relating droplet deformation to IFT using microfluidics has been reported by several sources. Deformation is achieved by passing droplets through an expansion, and examining the droplet deformation in a fluid flow field. The most common chip design includes a narrow channel expanding to a larger chamber. The number of chambers varies between 1 and 121, as shown in Figure 2.5.1. The droplet generation most commonly used is the flow-focused geometry. The chips also include a side stream of continuous phase in order to space the droplets and control the speed.[16;4;17;18]

Figure 2.5.1: Chip design with larger chambers connected by narrow channels. The number of chambers vary in the published literature.

In the following sections, four publications showing the relationship between interfacial tension and droplet deformation are reviewed. Note that the symbols used vary between the publications. Most importantly, the deformation is noted using both D and δ_{max}.

2.5.1 Cabral and Hudson[16]

One approach for the determination of interfacial tension is proposed by Cabral et al. Based on the dynamics and retraction of an isolated droplet subject to an unbounded extensional flow and making the appropriate simplifications and adjustments Cabral et al. reached the following equation:

$$\alpha\eta\left(\frac{5}{2\hat{\eta}+3}\dot{\epsilon} - u\frac{\partial D}{\partial x}\right) = \sigma\left(\frac{D}{a_0}\right) \tag{2.5.1}$$

where η is the viscosity of the continuous phase, and $\dot{\epsilon}$ is the extension rate and defined as $\frac{\mathrm{du}}{\mathrm{dx}}$. σ is the interfacial tension, D is the deformation and a_0 is the equilibrium radius. α is an 'effective' viscosity as defined below in Equation 2.5.2.

$$\alpha = \frac{(2\hat{\eta}+3)(19\hat{\eta}+16)}{40(\eta \hat{+} 1)} \qquad \text{where } \hat{\eta} = \frac{\eta_d}{\eta_c} \tag{2.5.2}$$

Plotting the right hand side of Equation 2.5.1 against D/a_0 yields the interfacial tension as the slope.

Ethylene glycol (EG) in polyphenylmethylsiloxate (PPMS) or water and EG in PDMS oil was used in this publication.[16]

2.5.2 Brosseau et al.[4]

Brosseau et al. expected two dimensionless numbers to govern the system. The capillary number, Ca, and a geometrical number, R*. The definitions of these are given in Equation 2.5.3.

$$Ca = \frac{\eta U}{\gamma} \qquad\qquad R^* = \frac{2R}{W} \tag{2.5.3}$$

where η is the viscosity of the continuous phase, U is the droplet velocity and γ is the interfacial tension. R is the radius of the droplet and W is a typical length. The width of the narrow channels is used.

Brosseau's chip has a different configuration than the one used in this experiment. The main difference of importance is the inclusion of a side stream to allow spacing of droplets. This allows for good control of both droplet size and velocity as they can be set separately. Two experiments were conducted:

1. Fixing the droplet size and varying the velocity and interfacial tension gives the opportunity to plot capillary number against maximum deformation. When plotted on a log scale the data collapse and yield a power law: $\delta_{max} \sim Ca^{2/3}$.

2. A second experiment was then conducted where the velocity was fixed and the droplet size and IFT were varied. A plot of $\delta_{\mathrm{max}}/\mathrm{Ca}^{2/3}$ against R^* yields an exponent for R^*.

The following equation was then found.

$$\delta_{max} = 0.8 Ca^{2/3} R^{*3.7} \tag{2.5.4}$$

As shown in Equation 2.5.3 the capillary number is a function of interfacial tension. Solving Equation 2.5.4 with respect to the interfacial tension yields the following model:

$$\gamma = \eta U_{defo} \left(\frac{0.8}{\delta_{max}} \right)^{1.5} R^{*5.5} \tag{2.5.5}$$

where U_{defo} is the velocity at the location of the maximum deformation, and δ_{max} is the maximum deformation. The interfacial tension can then be calculated given the information retrieved from microfluidic experiments.

The aqueous solution used was Millipore water-ethanol mixtures. The dispersed phase was fluorinated oil stabilized by perfluorinated surfactant molecules, a non-ionic tri-block-polymer.

2.5.3 Kong et al.[17]

A method based on Brosseau's work was used in the work by Kong et al. A similar chip design was used. The model reached in this work is shown in Equation 2.5.6.

$$\delta_{max} = \delta_{max}^0 \cdot Ca^{0.5} R^{*1.1} + 0.016 \tag{2.5.6}$$

Three surfactants were used: surfactin, 5-SCBS and 8-SCBS. Hexadecane was used as the dispersed phase.

2.5.4 André et al.[18]

Although André et al. did not calculate interfacial tension they derived a similar expression as Brosseau:

$$\delta_{max} = 0.7 Ca^{0.6} R^{*2.5} \lambda^{-0.1} \tag{2.5.7}$$

where $\lambda = \eta_{\mathrm{d}}/\eta_{\mathrm{c}}$. The function has been fitted to experimental data using a mean square procedure.

Water-glycerol mixtures were used as the continuous phase. The dispersed phase was a silicone oil stabilized by DTAB.

2.5.5 Summary and comparison

The method by Brosseau have been used in several papers. The works differ in both chemicals and equipment resulting in different parameters in the model. Some important parameters are compared in Table 2.5.1. The numerical exponent varies for both chip dimension and composition of phases. The model must therefore be fitted for each system, and no universal model is achieved at this point.

Table 2.5.1: Summary and comparison of literature. Papers are given in order of publication year. The number of chambers, the frame rate and the number of droplets captured is given. The ratio is the ratio between the width of the channel and the chamber. The exponents in the derived model are given.

	Chambers	**Frame Rate** [fps]	**Count**	**Ratio**	**Model** **Ca**	R*
Cabral[16]	3	-	-	0.33	-	-
Brosseau[4]	121	9100	10	0.33	0.66	3.7
Kong[17]	110	1500	-	0.33	0.5	1.1
André[18]	1	4000	3	0.39	0.6	2.5
Selvik	36	8500	50-150	0.25	-0.0766	-0.0874

It should be noted that all published literature defines the deformation as $D = (L - l)/(L + l)$ where L is the major axis and l is the minor axis. In this thesis, the deformation is defined as the aspect ratio of the width and the height of the droplets, $AR = W/H$. The droplets are captured in images yielding two dimensions. The y-direction is defined as the height. There have not been found any differences between the two definitions.

Some weaknesses in the published literature have been identified. The chemicals used in some of the published papers on microfluidic IFT represent ideal systems. Fluorinated oil and perfluorinated surfactants are used by Brosseau. Error analysis is also lacking in the presented results. Accuracy in the image analysis and the specific algorithms used are not presented. Sensitivity analysis of the parameters in the final model has not been published and the validity of the final model is therefore not determined.

Chapter 3

Method

3.1 Ring tensiometer

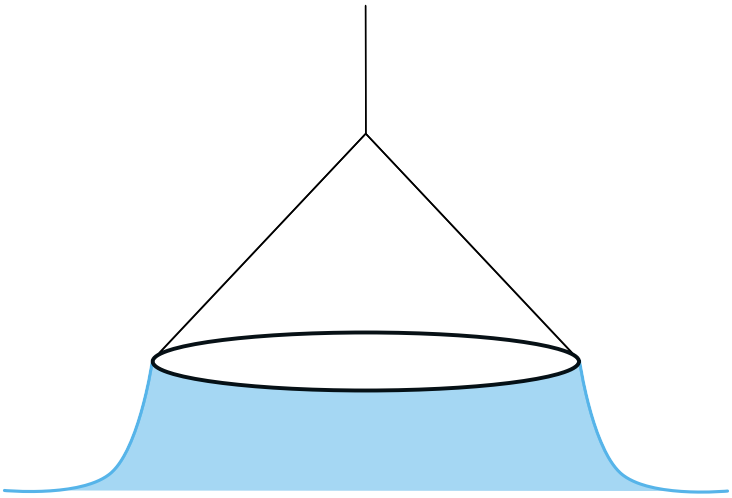

Figure 3.1.1: Sketch of the ring tensiometer.

The ring tensiometer, as described in Section 2.4, is one established method of IFT measurements. A platinum ring is used as the probe as shown in Figure 3.1.1.

The detachment force from the ring can be estimated as the interfacial tension multiplied by the periphery of the surface. The mass and buoyancy of the ring must also be considered. Equation 3.1.1 show the equation.

$$F = w_r - b + 4\pi R\gamma f \tag{3.1.1}$$

where F is the force, w_r is the weight of the ring, b is the buoyancy, R is the radius and γ is the interfacial tension. f is a correction factor.[19;20] The correction factor must be included due to the irregular shape of the interface and the direction of tension forces.

3.2 Microfluidics

Microfluidics is an emerging technology that deals with the manipulation of flows in micro channels. Specially manufactured chips with desired geometries and precise syringe pumps are used to flow fluids through the chip. Most common is droplet-based microfluidics where one phase is dispersed as droplets in another. Microfluidics has earned the name "lab-on-a-chip" due to the large variety of chip designs available. Depending on the need of the researcher the chip can include several components. In the following sections some aspects of the microfluidic methodology will be presented.

3.2.1 Droplet generation

Droplet-based microfluidics is a useful approach for the examination of small, discrete volumes. With droplets below 100 µm, the mass and heat transfer are enhanced compared to larger volumes.[21;3] The droplet generation geometry can vary, but cross-flow, flow-focus, and co-flow are some of the most common geometries. These are shown in Figure 3.2.1.

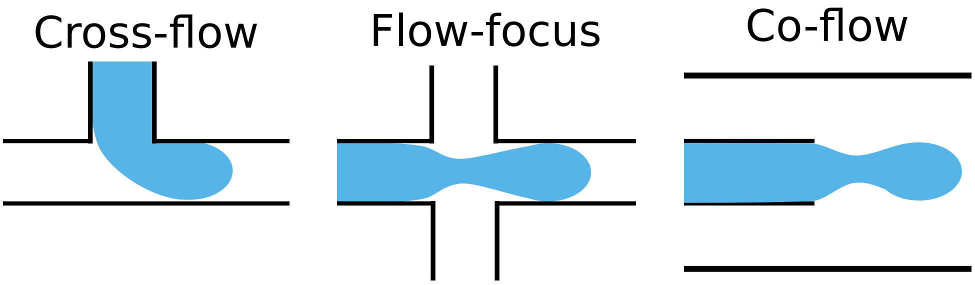

Figure 3.2.1: Microfluidic droplet generation. Cross-flow, flow-focus, and co-flow.

Droplets are formed by taking advantage of shear forces between the continuous and dispersed phases. As the disperse phase fills the channel a pressure drop is formed due to the hydraulic resistance to flow around the droplet. This force against the neck of the droplet causes it to detach.[3;22] A cross-flow droplet generation geometry was first reported by Thorsen et al.[23] A 90°angle is used and the droplet size depends on the flow of continuous and dispersed phase, as well as the respective fluid properties.[3]

3.2.2 Deformation

Droplet deformation is achieved by a series of expansions and constrictions. As the flow channel expands from a narrow channel to a larger chamber the divergent flow generates viscous stress.[24] A similar phenomenon can be seen in the constrictions. The flow profile deforms the droplets, and the deformation is a function of velocity, IFT, and droplet size. High interfacial tension yields a small deformation and a more rigid droplet. Low IFT, however, allows for a larger deformation. This can be seen in Figure 3.2.2.

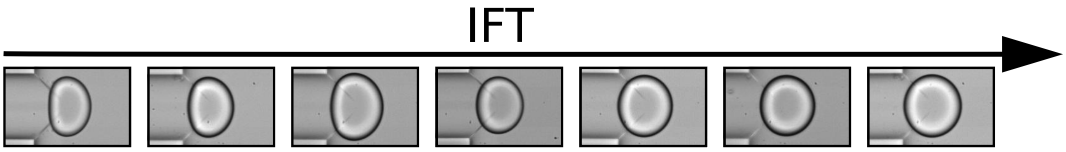

Figure 3.2.2: Deformation of the droplet as a function of interfacial tension.

3.2.3 Image analysis

Images captured using the microfluidic method must be analyzed. In this thesis, a neural network developed at Ugelstad Laboratories, NTNU, was used. It is based on yolov5, an object detection algorithm. This model, first developed by Redmon et al. uses four convolutional layers and two connected layers to construct a bounding box around the detected object.[25] The image is divided into several sections and objects are detected within each section. The reader is advised to read the published article by Rutkowski et al.[26]

3.2.4 Training of neural network

The neural network was trained to improve the weights in order to enhance droplet detection. A selection of images was annotated manually using the open-source *LabelImg* interface retrieved from GitHub. Bounding boxes were drawn around droplets at different positions and states. Then the neural network was trained with the images and tested on a validation set. Results were compared to image analysis done using *ImageJ* and the best weights were chosen.

Four image analysis methods are compared in the next paragraphs:

small	New weights using the small version of yolov5
large	New weight using the large version of yolov5
old	Old weights developed at Ugelstad
ImageJ	Analysis with ImageJ as reference.

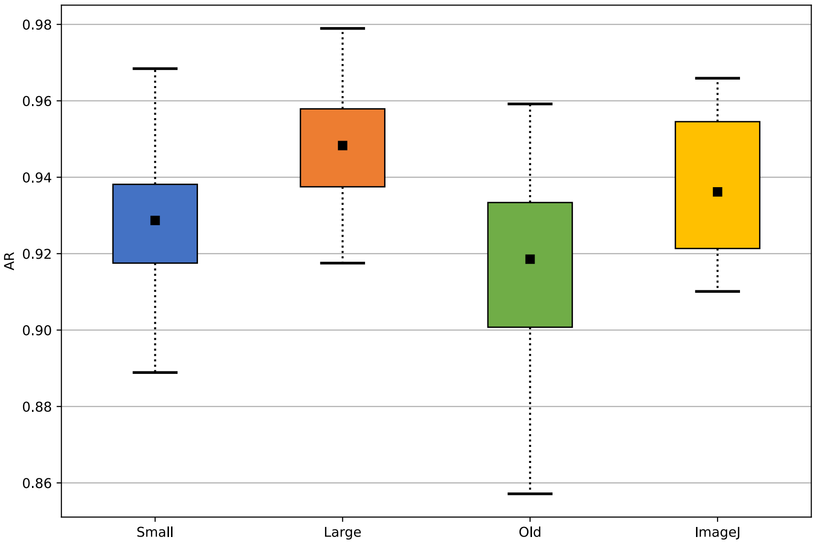

Figure 3.2.3: Comparison of image analysis using different weights for the neural network and ImageJ as reference.

Figure 3.2.3 show the average minimum AR of the droplets found by each of the methods listed above. It is clear that the old weights had a larger standard deviation. It was also seen that the old model would detect satellite droplets whereas the new models are not trained to look for smaller droplets and are therefore not detected. Image J shows a tight distribution and is used as a reference here. The method is not used as it is time-consuming. The new models have a tighter distribution and are therefore preferable. Figure 3.2.4 show the distribution for the models. Both the new models show a normal distribution. The larger model has more layers and a tighter distribution. It is therefore deemed the best for the applications in this thesis.

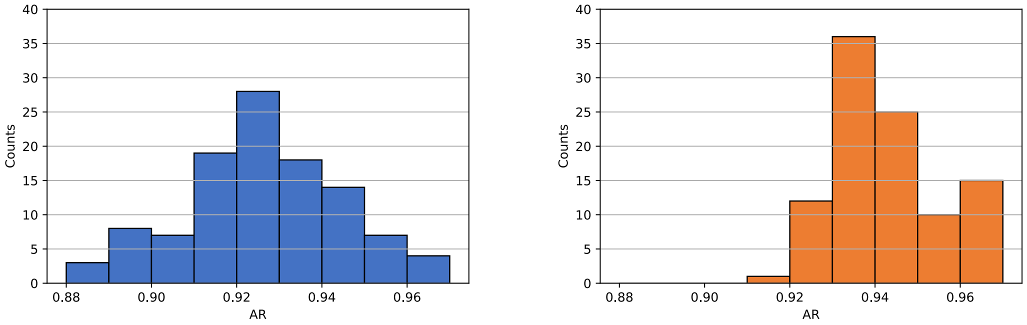

(a) Small yolov5 model **(b)** Large yolov5 model

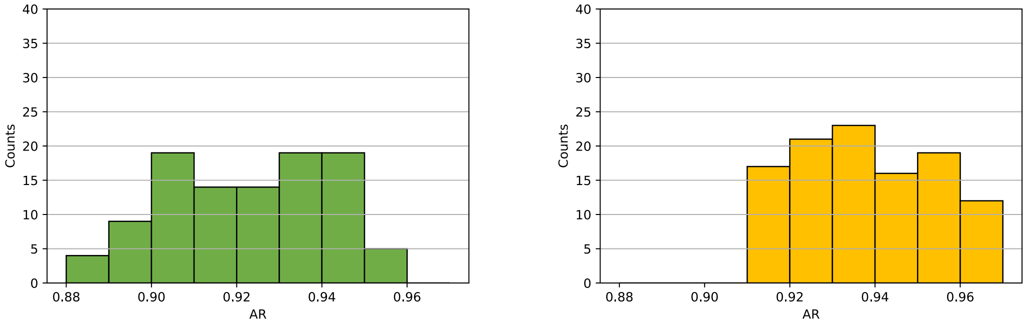

(c) Old yolov5 model **(d)** ImageJ

Figure 3.2.4: Histograms showing the distribution of maximum deformation detected for the four different image analysis methods.

Chapter 4

Experimental

4.1 Ring tensiometer

Interfacial tension measurements were made using a *Sigma Attention 701 Ring Tensiometer* manufactured by Biolin Scientific. The instrument includes a movable platform and a hook connected to a scale. A vessel with the solution of interest was placed on the platform and a ring was hung from the hook. As the ring was pulled from the interface the force was measured and the interfacial tension can be calculated.

Before all measurements, a test was made to ensure the instrument operated correctly. The surface tension of methanol was measured and compared to the literature value.[27] If the measurements were outside a range of ±0.5 mN/m the ring and vessel were cleaned and a new test was made. The vessel was filled with 15 ml of the aqueous phase as the heavy phase. Then 15 ml dodecane was carefully added to the top using an automated pipette. The ring was lowered into the light phase and placed a few millimeters above the interface. Parameters like run time, delay between measurements, and dwell down were configured and the experiment was started. In the first phase of the experiment the scale was zeroed and the ring was lowered to the interface. When the interface was detected the ring moved below the interface and the measurements began. The platform was moved down to let the ring pull the interface up through the light phase. When the maximum was detected the ring was lowered (by rising the platform) below the interface and a new measurement was started. The IFT decreases as time passes due to the adsorption of surfactant to the interface. This can be seen in Figure 4.1.1. In the span of 24 hours over 700 measurements were made. The equilibrium value and standard deviation were calculated as an average over the last third of measurements, marked by a blue square in the figure. The measurement was repeated for a range of surfactant concentrations.

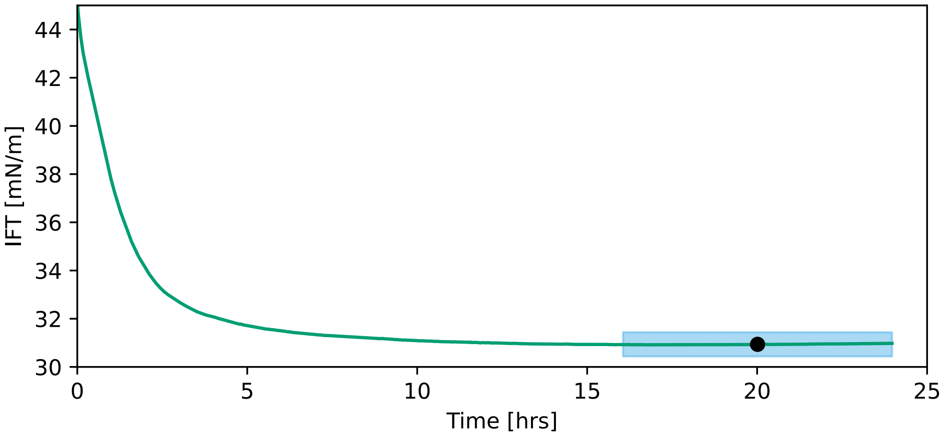

Figure 4.1.1: Dynamic interfacial tension measurement of dodecane and a 0.5 μM Tween 20 solution. The IFT decreases as time passes due to the diffusion of surfactant to the interface. The equilibrium value is shown in black. The value is calculated as the average of the last third of the measurement, highlighted in blue.

4.2 Microfluidic setup

The microfluidic platform is located at Ugelstad Laboratories at NTNU.

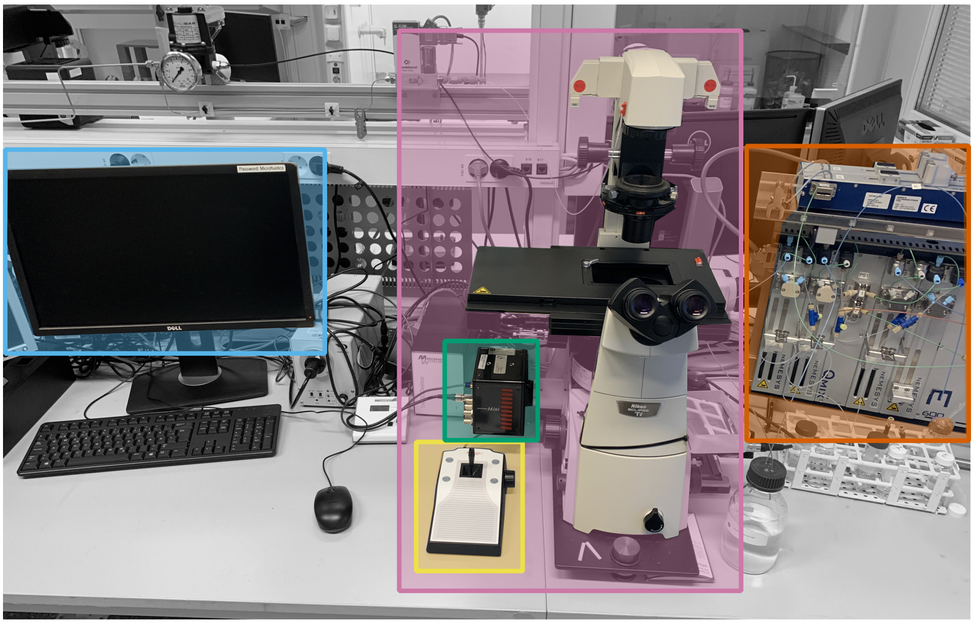

Figure 4.2.1: The microfluidic setup. The computer (●) with software controlling the camera (●), stage (●), and the pumps (●). The chip is mounted to the stage on the inverted microscope (●).

4.2.1 Microscope

The microscope used is a *Nikon Ti-U Inverted Microscope.* As the name suggests the microscope is inverted, meaning the light source is located on the top and the objectives are placed below. The reason for this is to avoid the inlet tubing blocking the view of the chip. A 20x objective was used and the light source was set to 14% intensity. A diffusing filter was applied to distribute the light and a ND2 (Neutral Density, 1/2) filter was used to adjust the brightness.

4.2.2 Stage

The chip was mounted to the microscope on an automated stage. The stage was connected to *Tango Desktop* by Märzhäuser Wetzlar. A joystick was then used to control the movement of the stage. The software offers several movement options. The *position list* option was used to save certain positions and cycle through the given positions. This was useful when wanting to capture the same areas for different conditions.

4.2.3 Chip

The chip design is central when working with microfluidics. The design used in this work consists of a series of successive chambers. Two chips have been used; TJ22 and FF36. The letters in the name indicate the droplet formation geometry; *T*-*J*unction and *F*low *F*ocusing. While the number refers to the number of successive chambers. Chip FF36 has 3 inlets which will, for simplicity, hereafter be referred to as in accordance with Figure 4.2.2. In TJ22 there are only 2 inlets; one for the continuous and one for the dispersed phase. Both chips include a number of successive chambers with the same dimensions. Figure 4.2.3 shows the dimensions of the chip. A secondary inlet for the continuous phase marks the major difference between the chips used in literature and the one used in this thesis.

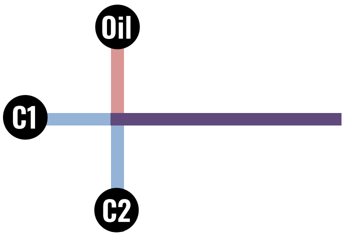

Figure 4.2.2: C1 and C2 is the inlet for continuous phase while the oil inlet is for the dispersed phase.

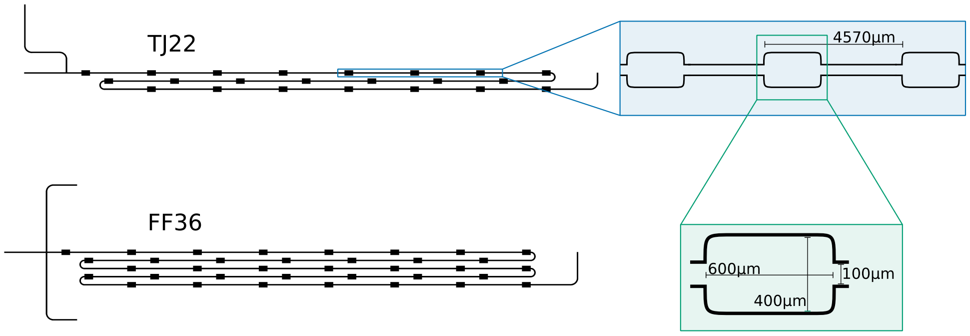

Figure 4.2.3: Chip dimensions and design. The chambers are spaced 4.6 mm apart with a channel 100 µm wide. Each chamber is 600 by 400 µm. The depth of the chip is 45 µm throughout the entire chip.

4.2.4 Pumps

Cetoni syringe pumps were used to control the flow. Low-pressure horizontal pumps were chosen to better control low flows. The flows were controlled using the *Qmix Elements* software and ranged from 0.5 to 110 µL/min. The pumps were connected to the chip with FEP tubing with an outer diameter of 1.6 mm and an inner diameter of 0.25 mm. A filter was also added to the aqueous streams to prevent dust and particles inside the chip, from obstructing the flow.

4.2.5 Chemicals

The dispersed phase used in this work is dodecane. The continuous phase was an aqueous solution of MQ water and Tween 20. Tween 20 is a non-ionic surfactant with an average molecular weight of 1228 g/mole.[11] A stock solution of 0.5mM was prepared and diluted tenfold. The CMC of Tween 20 is 0.05 mM and the viscosity is reported to be 1.0 mPa s at the concentrations used.[11;28]

4.2.6 Image capture

The microscope is connected to a camera and a light source. *Fastcam Mini AX*, a high-speed camera by Photron, is used. The camera options used for most experiments are shown in Table 4.2.1. The main goal of the camera settings was to capture the droplet deformation with a sharp image. The frame rate was increased to capture the deformation, while the shutter speed was decreased to avoid a blurry image. The light and filters were used to achieve a good contrast between the droplets and the background. The resolution was chosen to capture the inlet of a chamber, and reduce the amount of noise. The objective chosen was 20x as the droplets are in the size range of 80 ± 10 µm.

33 partitions were made such that each recording lasted 0.83 seconds. This allowed for capturing between 50 and 200 droplets depending on the droplet generation frequency and velocity. The data sets included 7058 images.

Table 4.2.1: Summary of camera settings.

Image capture	
Objective	20x
Frame rate	8500 fps
Shutter speed	1/90 000 sec
Resolution	128 x 384 pixels
Light intensity	14%
Filters	Diffuser and ND2
Px/µm	1.03

4.2.7 Cleaning

After each experiment, the set-up was cleaned. Syringes and tubing with aqueous solutions were cleaned with MQ water. Syringes and tubing with oil phase were cleaned with xylene and the syringes were further cleaned with isopropanol. Syringes, tubing, fittings, and filters were left in an oven at 55℃ overnight to let solvents fume off and the water evaporate.

The chips went through three cleaning cycles in an ultrasonic bath. Each cycle lasted 15 minutes and the cleaning solutions were 2% v/v Decon 90, isopropanol, and MQ water. In cases where the chip needed further cleaning Hellmanex at 50°C was used before the normal cleaning cycle.

4.3 Data analysis

4.3.1 Neural network

Image analysis was carried out using a specially trained neural network. The network is based on the yolov5 model. The result of the analysis gives the output shown in Table 4.3.1 and visualized in Figure 4.3.1. The output is saved as a .json file so a developed script transforms the data into a .csv is used. The analysis is made using *DataFrames* in the *Pandas* package for python.

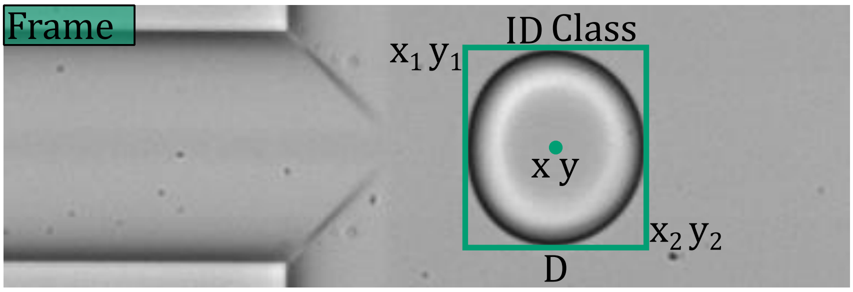

Figure 4.3.1: Visual representation of the output from the neural network. x and y is the position of the center of the bounding box. x_i and y_i is the position of the corner. D is the diameter calculated as the average of the width and height of the box.

Table 4.3.1: Output from the neural network.

Neural Network output	
Class	Only one class is used
Droplet ID	Given ID to differentiate droplets
Frame	Frame number where droplet appears
X	X position of the center of droplet
Y	X position of the center of droplet
D	Droplet diameter
X1	X position of upper left corner
Y1	Y position of upper left corner
X2	X position of lower right corner
Y2	Y position of lower right corner

4.3.2 Data processing

The aspect ratio, AR, is used as a measure of deformation. It is defined as the width of the droplet in the x-direction divided by the height of the droplet in the y-direction. From the output from the neural network, the aspect ratio is calculated as shown in Equation 4.3.1.

$$\mathrm{AR} = \frac{X_2 - X_1}{Y_2 - Y_1} \tag{4.3.1}$$

As the droplets move through the chip the AR varies. Plot **a)** in Figure 4.3.2 show AR as a function of position in the chip. Single droplets are plotted separately. At maximum deformation, a local minimum can be seen in the AR. The minimum value for each droplet was identified, and an average is reported as the AR of the experiment. The standard deviation is calculated.

Plot **b)** in Figure 4.3.2 show the diameter as a function of x-position. An average diameter of the droplets is given by the neural network. It is calculated as the average of the width and height of the bounding box. The droplet diameter was found by removing non-spherical droplets. A spherical droplet has an AR value of 1, so by removing all droplets with an AR outside 1 ± 1% only spherical droplets remain. Droplets in the channel and around the deformation were removed based on x-position. An average of the diameter over the remaining detections yielded the diameter and standard deviation.

Plot **c)** in Figure 4.3.2 shows the velocity of a droplet as a function of position. The velocity is calculated as the change in position divided by the change in time as shown in Equation 4.3.2.

$$U = \frac{\Delta s}{\Delta t} \tag{4.3.2}$$

The time is calculated from the known frame rate of the camera and the number of frames between detections of the droplet. The velocity profile at the expansion has the shape of an S-curve. The sigmoid function with a similar profile is given below.

$$y = a + \frac{L}{1 + e^{k(x - x_0)}} \tag{4.3.3}$$

a, L, k and x_0 in Equation 4.3.3 is fitted to the velocity profile. The regression is shown with a green line in plot **c)** in Figure 4.3.2. The velocity at the maximum deformation is retrieved based on the x-position. The standard deviation is calculated based on data points close to the x-position of maximum deformation. Data in a 5% range to either side are included. The error bars in the plot show the standard deviation for the velocity and the range used to calculate the error in the x-direction.

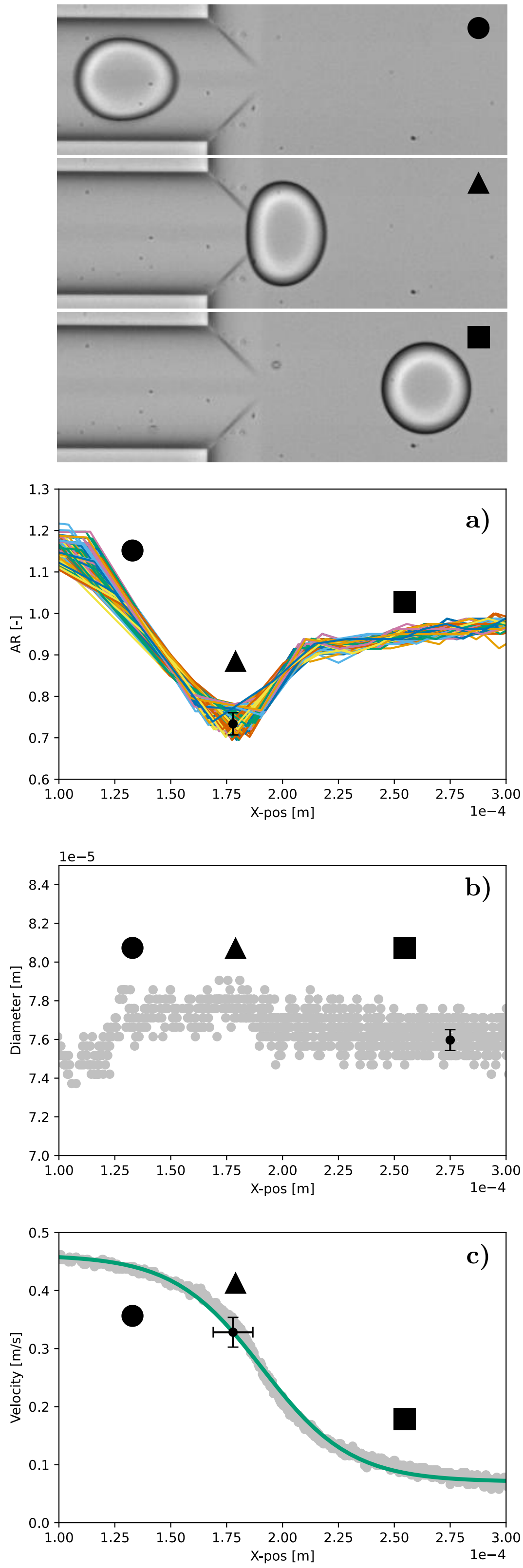

Figure 4.3.2: Calculated deformation (**a**), diameter (**b**), and velocity (**c**) of droplets in the channel (●), at maximum deformation (▲), and when relaxed (■). The reported values are shown in black with the corresponding standard deviation.

The scripts used for data extraction and analysis can be found in Appendix D. The script includes, in addition to the calculations described above, formatting like removing partially detected droplets, converting lengths from pixels to SI-units, and re-labeling duplicate indexes and

Chapter 5

Results and discussion

5.1 Ring tensiometer measurements

Measurements from the ring tensiometer were plotted with the concentration on a log scale. The data were then fitted to a second-degree polynomial function below CMC and a linear function above CMC. The functions are shown in Equations 5.1.1 and 5.1.2 respectively.

$$\textit{Below CMC} \quad \mathrm{IFT} = 5.41983 \cdot \log{(C)}^2 + 12.1122 \cdot \log{(C)} + 14.0443 \qquad R^2 = 0.92 \tag{5.1.1}$$

$$\textit{Above CMC} \quad \mathrm{IFT} = -1.35034 \cdot \log{(C)} + 5.61615 \qquad R^2 = 0.88 \tag{5.1.2}$$

The raw data and the fit can be found in Figure 5.1.1

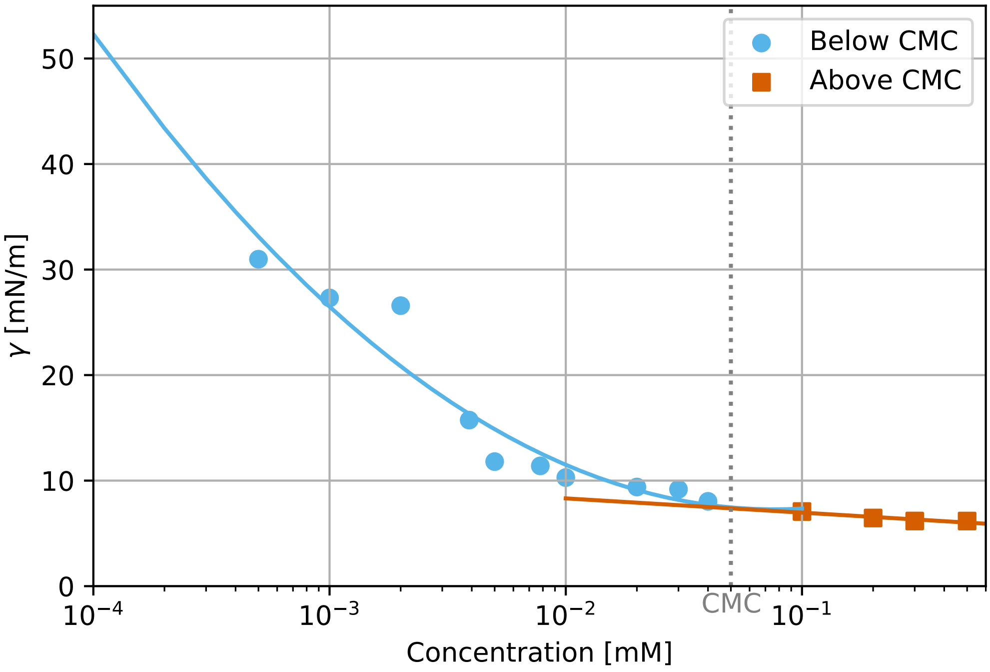

Figure 5.1.1: Interfacial tension of the Tween20-Dodecane system. The measurements were obtained using a ring tensiometer. The standard deviation is not included as it is < 0.5 mN/m for all points. CMC is marked by the dotted line at 0.05mM. Points above and below CMC are colored and marked with squares and circles respectively.

5.2 Microfluidic model development

In the following section the model development will be described. The data is unless otherwise specified, taken from the last chamber of the chip to be as close to equilibrium as possible.

5.2.1 Experimental

As seen in Section 2.5 most of the methods reporting microfluidic interfacial tension are based on the work of Brosseau et al. The method developed by Brosseau relies on control over both droplet size and velocity. To find a model relating deformation to interfacial tension, two experiments were made with solutions of varying, known, interfacial tensions.

1. **Fixed size** for a variety of velocities. This will yield a relation between deformation and the capillary number.
2. **Fixed velocity** for a variety of droplet sizes. This will yield a relation between droplet size and deformation.

Brosseau achieved this by using a second inlet for the continuous phase to space and speed up the droplets. This gave the opportunity to vary droplet size and velocity independently. The chips used in this work do not have this secondary inlet. This small change in chip design proved a big challenge, as the droplet size and speed are strongly interconnected. Several experiments were made to better understand the flow patterns and the influence of the different flows on droplet formation and speed.

The velocity is governed by the flow of the continuous phase. By keeping the flow of the continuous phase fixed and varying the flow of the dispersed phase it was possible to make droplets of different sizes, moving at the same speed. Figure 5.2.1a shows the diameter as a function of the dispersed phase flow.

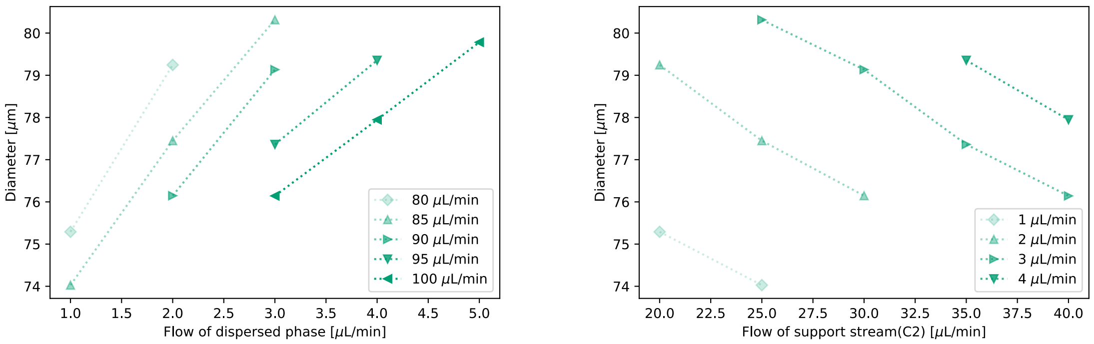

(a) Diameter as function of dispersed phase flow. The flow of the continuous phase is given in the legend.

(b) Diameter as function of secondary flow(C2). The flow of the dispersed phase is given in the legend.

Figure 5.2.1: Droplet size variation with flow conditions.

Control of the size of droplets at varying velocities proved a larger challenge. The size was reduced when increasing C2, as seen in Figure 5.2.1b It was hypothesized that by balancing the flow of the dispersed phase and the supporting continuous flow, droplets of the same size moving at different velocities could be achieved. A series of experiments were made as shown in Figure 5.2.2. The experiments yielding droplets of the same size were used in the model development. A range of 2 μm was accepted, as shown by the green band in the figure below.

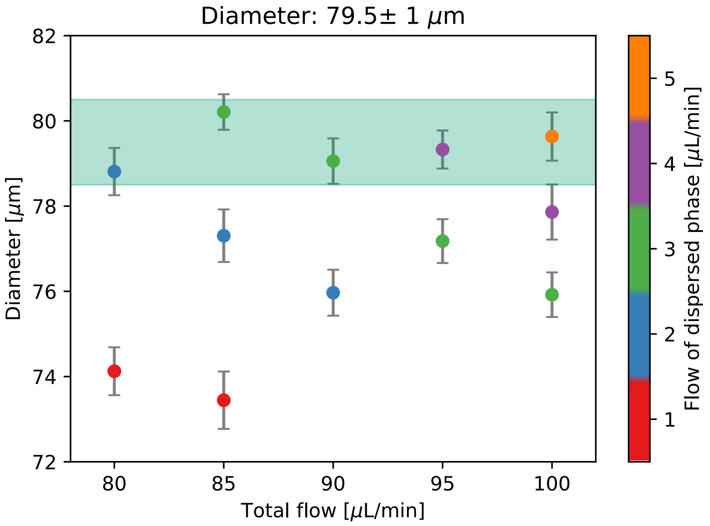

Figure 5.2.2: Plot showing droplet size dependence on both the continuous and dispersed phase flow. The total flow is the sum of the main flow (C1) and a side flow (C2). The main flow (C1) is kept constant and equal to 60 µL/min for all experiments. Colors signify the flow of the dispersed phase (OIL). The green band represents an accepted range of 2 µm.

A total of 74 experiments distributed between 7 concentrations of surfactant were used to fit the model. The raw data used for the model fitting can be found in Appendix C and more details about the experimental work can be found in Appendix A. Figure 5.2.3 shows a histogram of the velocities and number of detected droplets used to fit the model.

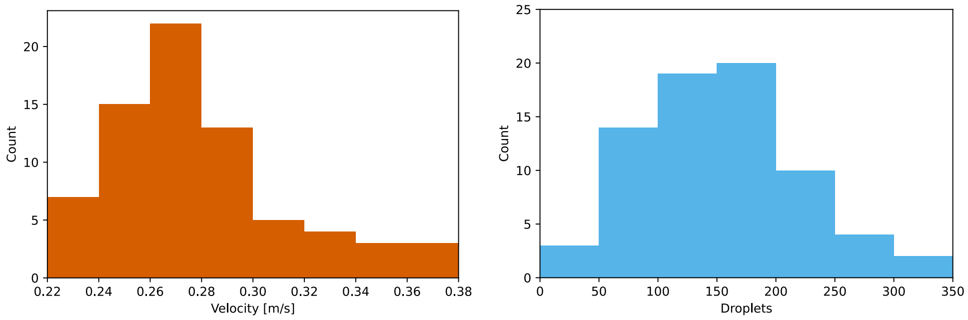

Figure 5.2.3: Histogram of the velocities and droplets used to fit the model.

5.2.2 Experimental limitations

In the experimental work several limitations were identified. In the following section, some are highlighted. Figure 5.2.4 gives a visual representation of the limitations. The droplet size and speed depend on the flow of the continuous and dispersed phases. The chosen flow rates are found empirically to work for the system in question, but may vary with chip design and/or chemicals. It must also be acknowledged that the flows chosen in this work are not unique and that other parameters may improve the work. However, it is useful to understand what criteria the conditions must meet and what limitations are in place.

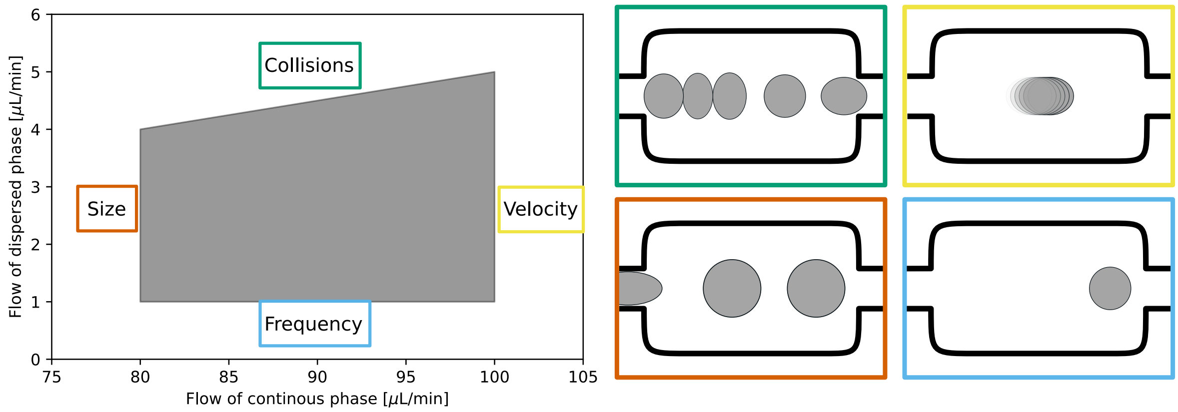

Figure 5.2.4: Outline of the working space in the system used in this thesis. The graph on the left shows the flow of continuous and dispersed phase. The figures on the right show the corresponding issues.

The continuous phase flow is limited by droplet size and velocity. Assuming the dispersed flow is constant, a reduction in continuous phase flow will yield larger droplets. Droplets may then be deformed in the narrow channel between chambers, which may, in turn, affect the deformation of the droplet. A lower limit of 80 µL/min is therefore chosen in this work (●). A high flow of continuous phase, on the other hand, will increase the velocity of the droplets. The challenge then is capturing the droplet clearly with the camera. A higher velocity would require a smaller shutter speed (●).

The lower limit of the dispersed phase flow relies on the syringe pumps. As the flow becomes very low, some unstable flows have been observed. There is also an issue with the number of droplets. As the dispersed flow is reduced the droplet generation frequency drop. This must therefore be compensated by increasing the length of the recordings. If the length of recording becomes very large this will propagate into the image analysis time (●). The upper extreme is limited by droplet crowding and collisions. If the droplet generation frequency increases droplets may collide in the chamber. Interactions between droplets may affect the deformation and must therefore be avoided (●).

Figure 5.2.4 gives an impression of the working space available for the system described in this thesis. Note that these limitations are not absolute and that there is some leeway in all directions.

5.2.3 Model development

For the experiments with constant velocity the deformation was plotted against the geometric factor R* on a log-log scale. Linear regression was carried out for each parallel by fitting an exponential function on the log-log scale. An average of the exponent (analog to the slope of the linear fit) was chosen as the fitted parameter. The plots showing the linear regression can be found in Appendix B.1.

Figure 5.2.5 shows the results for the fixed velocity experiments with the calculated exponent shown and plotted as guidelines. Small variation in capillary number can be seen, this is mostly due to the variation in interfacial tension. The slope of the fit was found to be -0.0874.

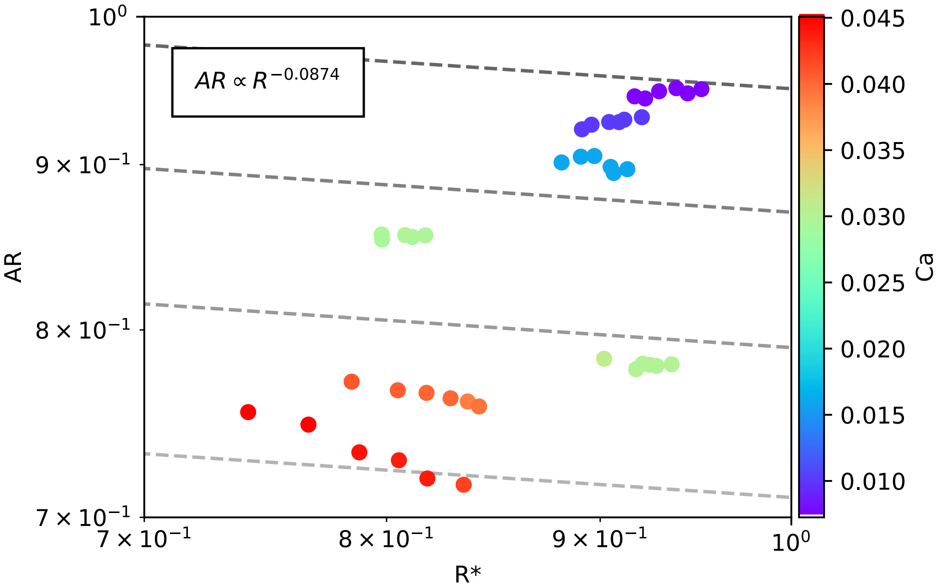

Figure 5.2.5: Experiments with fixed velocity. Deformation is plotted against R* on a log-log scale.

A similar plot was made for the experiments with constant sized droplets at different velocities. The plot can be found in Figure 5.2.6. In this case, the capillary number is plotted against the deformation. The slope was found in the same way as for R* and was found to be -0.0766.

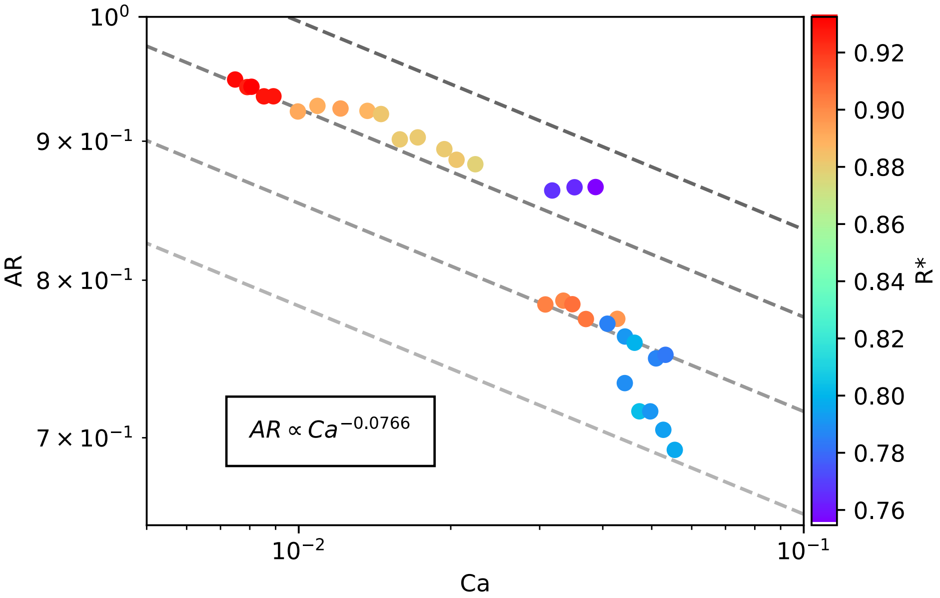

Figure 5.2.6: Experiments with fixed droplet size. Deformation is plotted against the capillary number on a log-log scale.

It should be noted that the droplet size within each series is constant, but not between parallels. This is due to the limitations of the chip design. This is also the reason an average of the slopes for each regression is chosen. The series in them-self are not numerically comparable, but the trend is still representative.

The model was then fitted by plotting Ca ·R* with the determined exponents against deformation. It can be seen in Figure 5.2.7 that the data collapse on a line.

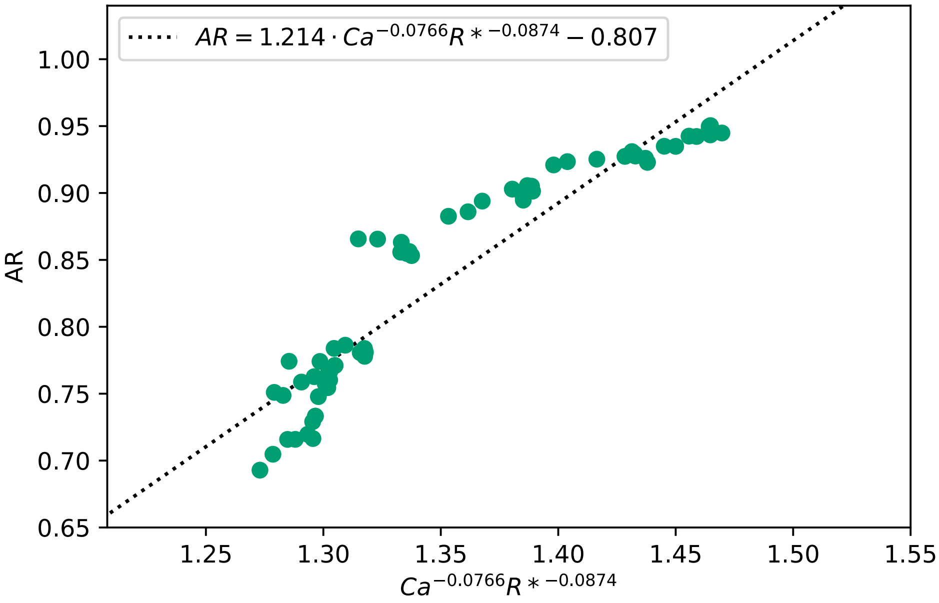

Figure 5.2.7: Collapse of data with the corresponding linear regression.

This yields the deformation as a function of R* and Ca. Solving the equation with respect to the IFT(γ) as shown below yields the final function shown in Equation 5.2.1.

$$\begin{aligned}
AR =& 1.214 \cdot Ca^{-0.0766} R^{*-0.0874} - 0.807 \\
\frac{AR + 0.807}{1.214 \cdot R^{*-0.0874}} =& Ca^{-0.0766} \\
\left(\frac{AR + 0.807}{1.214 \cdot R^{*-0.0874}}\right)^{-\frac{1}{0.0766}} =& \frac{\eta U}{\gamma} \\
\gamma =& \eta U \left(\frac{1.214 \cdot R^{*-0.0874}}{AR + 0.807}\right)^{-\frac{1}{0.0766}} \\
\gamma =& \eta U \left(\frac{0.5427 \cdot D^{*-0.0874}}{AR + 0.807}\right)^{-\frac{1}{0.0766}}
\end{aligned}$$

$$\boxed{\gamma = \eta U \left(\frac{0.5427 \cdot D^{-0.0874}}{AR + 0.8071}\right)^{-\frac{1}{0.0766}}} \qquad (5.2.1)$$

Where the coefficient 0.543 has the unit $[m^{0.0874}]$.

To check the accuracy of the model a parity plot is made. It can be found in Figure 5.2.8. The IFT found by the microfluidic model (γ_m) is plotted on the y-axis and the IFT from the ring tensiometer (γ_r) is on the x-axis. The line $\gamma_m = \gamma_r$ is shown as a guide for the eyes.

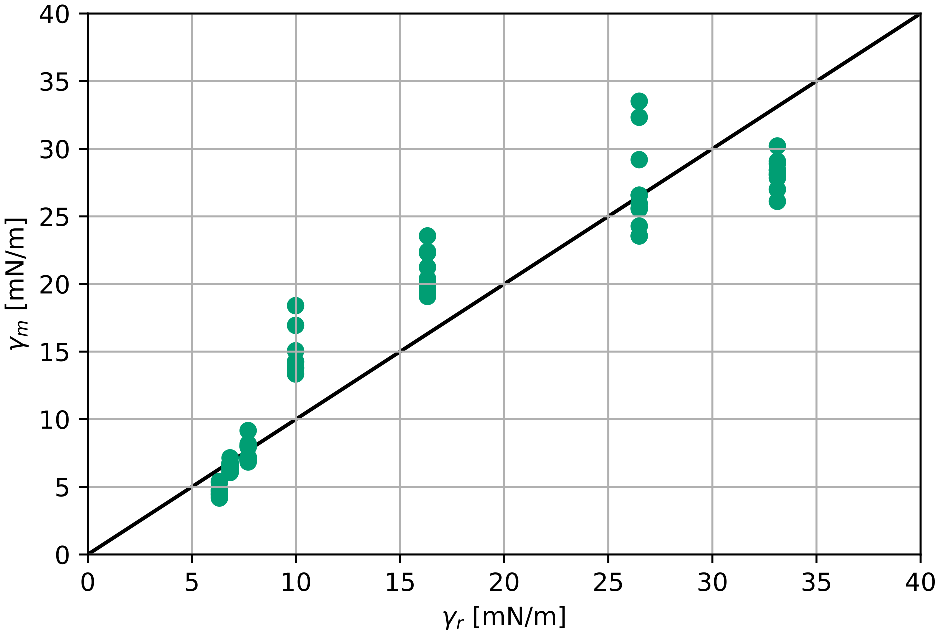

Figure 5.2.8: Parity plot of the ring tensiometer and the microfluidic model. The R^2-value of the data in relation to the parity line is 0.87.

It can be seen that the model is more accurate for systems with low IFT. For IFTs between 10 and 30, the model overshoots the value by between 2 and 10 mN/m. The reason for this may be that equilibrium is not reached. Diffusion to the interface is fast for high concentrations of surfactants, so at lower concentrations, more time is required to reach equilibrium. The residence time in the chip should therefore be increased. At high IFTs the deformation is very small so problems with detection may occur. This might explain why the model undershoots the value compared to the ring tensiometer at high IFTs. Additional plots and error calculations can be found in Appendix B.1.

5.3 Validation of model

In the following sections validation of the model will be presented.

5.3.1 Chip design

The model is fitted using the FF36 chip so it is useful to understand if the chip length affects the validity of the model. Figure 5.3.1 show the parity plot of the IFT from the model using the TJ22 and the FF36 chip. The major differences between the designs are the number of chambers and the droplet generation geometry.

For both experiments, the data represent the last chamber in order to be as close to equilibrium as possible. It must be noted that TJ22 only has 22 chambers, while FF36 has 36 chambers. Looking at the last chamber in each chip, therefore, means that the aging of the interface is further developed in FF36. This is the reason the IFT in TJ22 consistently is higher than in FF36. The results are nevertheless comparable. It can therefore be concluded that only the length of the chip and not the droplet generation plays a role in the model fit. However, it has not been explored whether other aspects such as the ratio between the channel and chamber and the dimensions and geometry of the chamber have an effect or not. It is hypothesized that a larger difference between channel and chamber will affect the deformation and the velocity profile.

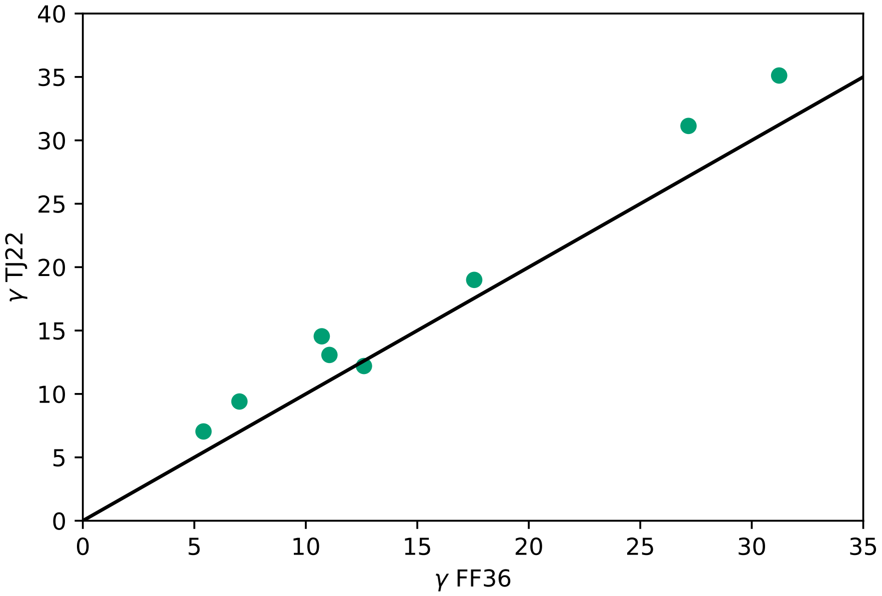

Figure 5.3.1: Parity plot between two different chip designs. Measurements are made in the last chamber of the chips.

5.3.2 Velocity

A narrow velocity range is used in the model development Figure 5.3.2 shows experiments outside the velocity range used in the fitting of the model. The equilibrium value from the ring tensiometer is given and the velocity range used to fit the model is shown in gray. The model has a higher accuracy at low IFT and is less accurate outside of the range used for the fit. This suggests that a larger velocity range should be chosen when fitting the model.

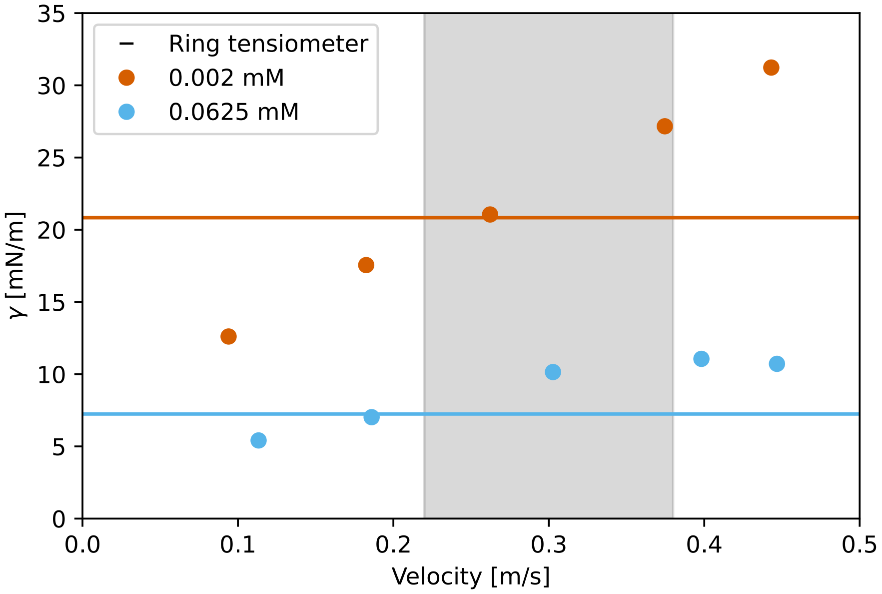

Figure 5.3.2: IFT plotted against velocity. The velocity range used to fit the model is shown in gray. The results of two concentrations are shown.

5.3.3 Error analysis

There are several error sources in the model. In the following paragraphs, some will be explored further.

All measured values have inherent uncertainty. This includes the ring tensiometer measurements. The Tween20-solutions used in the ring tensiometer were prepared by step-wise dilution. A stock solution was prepared using an analytic scale, and a graduated flask was used for the dilution. Errors in both the stock solution and dilution may be present. Measurements for a range of concentration have been fitted to a linear and a polynomial function above and below CMC respectively. The fits have R^2-values of 0.88 or higher. Some error in the fitting parameters must be considered. However, the errors in the IFT measured by the ring tensiometer is not assumed to be significant to the model uncertainty.

The capillary number is a function of viscosity, velocity, and interfacial tension. As the viscosity is assumed constant and a literature value is used, the error is assumed small and therefore neglected. As discussed the interfacial tension values have an inherent uncertainty due to the solution preparation and fitting parameters. The velocity is found by calculating the discrete velocity of each droplet from the distance traveled over time. Then a sigmoidal fit is made and the velocity at the maximum deformation is retrieved from the fit. The error is found to be approximately 10% on average.

The deformation has on average an uncertainty of 3% while the diameter has an uncertainty of 0.5%. The main error is caused by the resolution of the camera as well as the accuracy of the image analysis. The neural network returns positions and dimensions in integers with the unit pixels. With the camera parameters used in this thesis, one pixel is approximately equal to 1 µm. Changes on scales below 1 µm are therefore not captured.

5.4 Sensitivity analysis

To better understand the robustness and weaknesses in the model it is useful to do a sensitivity analysis. In this section, the sensitivity of the exponents of Ca and R^* will be discussed.

To better understand the significance of the exponent on the final model, a range of exponents was investigated. The exponents are determined by linear regression for 7 data sets and an average of the exponents is taken into the model. Exponents from each data set were used to supply a range of values. The exponents can be found in Table 5.4.1.

Table 5.4.1: Exponents for each data set in used in the sensitivity analysis. The exponents are shown in ascending order and the average is given.

								Average
R^*	-0.4643	-0.2402	-0.2351	-0.1018	0.0418	0.1514	0.2366	-0.0874
Ca	-0.2292	-0.1084	-0.0696	-0.0489	-0.0866	-0.0086	0.0149	-0.0766

5.4.1 Variation in R^* exponent

R^* is defined as diameter divided by a known width. Variations in R^* only stem from droplet size, since the width is constant. A larger droplet yields a larger R^* value. For each exponent of R^* the collapse of data were plotted and a linear regression was made through the data. The results are shown in Figure 5.4.1.

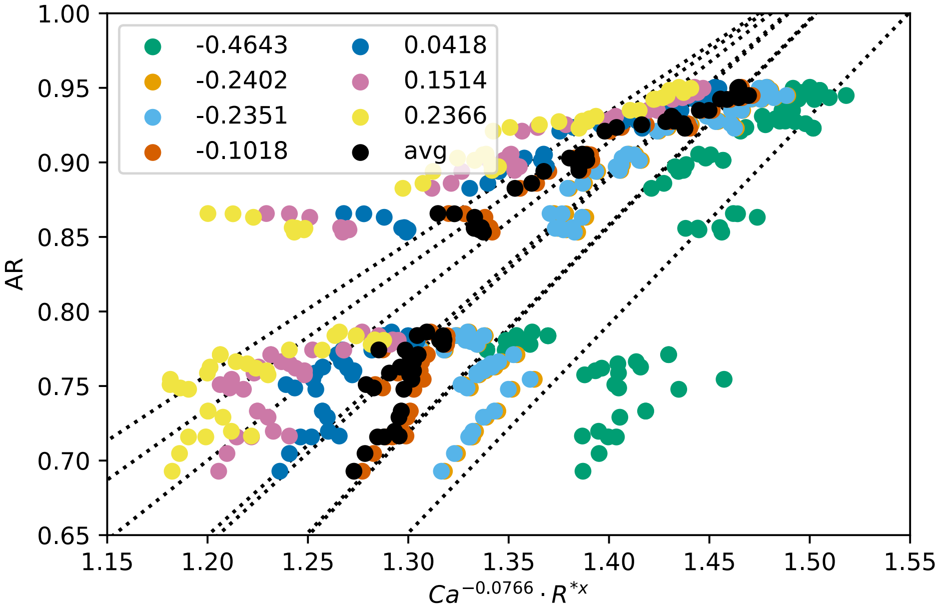

Figure 5.4.1: Collapse of data with variations in R* exponent. The exponent used for R* is shown in the legend and the black series represents the model. Dashed lines show the linear regression on the corresponding data series.

It can be seen that when the exponent is increased the intersect of the regression is increased. The intersection varies from -1.2 to -0.3. However, the slope shows little variation with values between 0.9 and 1.4.

With the linear fit found in Figure 5.4.1, a parity plot was made. It can be found in Figure 5.4.2.

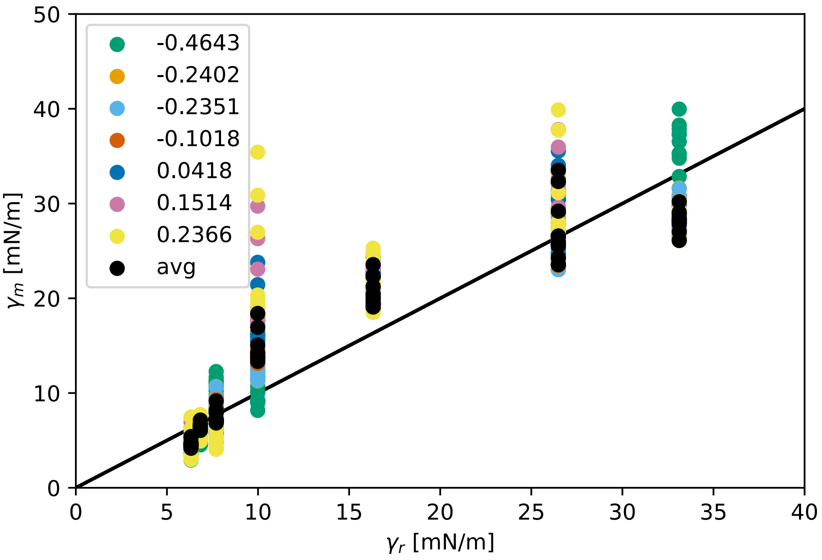

Figure 5.4.2: Parity plot for a range of exponents for R* . The solid line represents the parity line as a guide for the eye.

It can be seen that there is no large deviation from the model with the exponents. A larger spread for higher exponents can be seen. To better understand the accuracy the R^2-value in relation to the parity line was calculated. The values are shown in Table 5.4.2. It can be seen that the accuracy of the model is higher at lower values of exponents.

Table 5.4.2: R* -exponent and the corresponding R^2-value in relation to the parity line.

								Average
$\mathbf{R^{*x}}$	-0.4643	-0.2402	-0.2351	-0.1018	0.0418	0.1514	0.2366	-0.0874
$\mathbf{R^2}$	0.90	0.91	0.91	0.87	0.81	0.74	0.68	0.87

5.4.2 Variation in Ca exponent

The same analysis was made for the Ca exponent. The capillary number is a function of viscosity, velocity, and IFT, where the viscosity is considered constant. Ca is proportional to the velocity and inversely proportional to the IFT. The collapse of the data with the corresponding linear regression is shown in Figure 5.4.3.

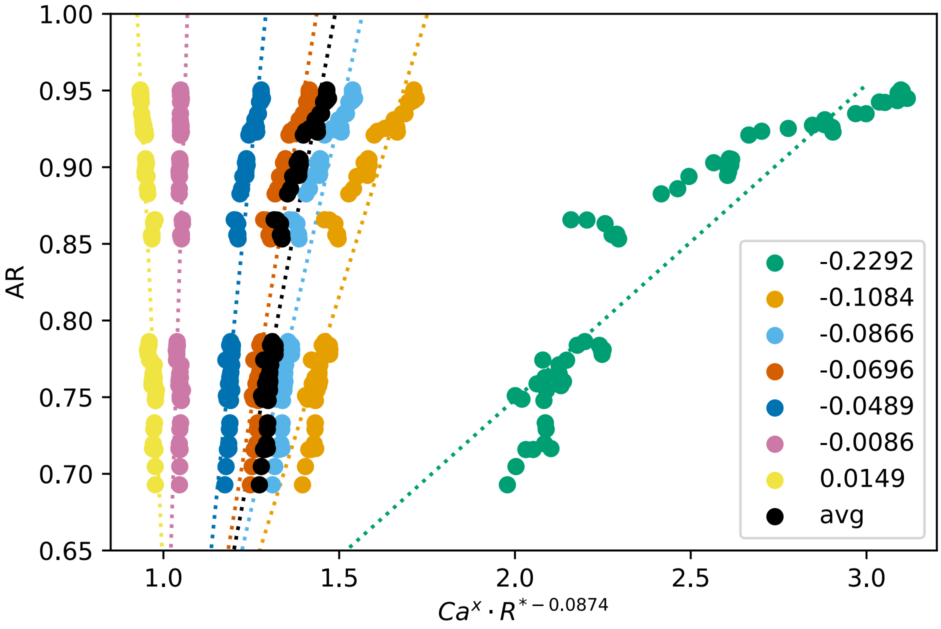

Figure 5.4.3: Collapse of data with variation in Ca exponent. The legend shows the exponents used in each series, and the black series represent the model. The corresponding linear regression is shown as dashed lines.

There is little variation in the slope when the exponent is between -0.1 and 0 as the slope varies from 0.2 to 2.2. For the highest exponent, a negative slope (-5) is seen while at the lowest exponent a slope of 7.4 is observed. The intersect varies between -1.9 and 0.3 for all but the two series with the highest exponent. When the exponent is -0.0086 the intersection is -7 while when the exponent is 0.0149 the intersection is 5.6. Regardless of these outliers the average lies within the trend seen. With the linear fits shown in Figure 5.4.3, the parity plot is shown in Figure 5.4.4.

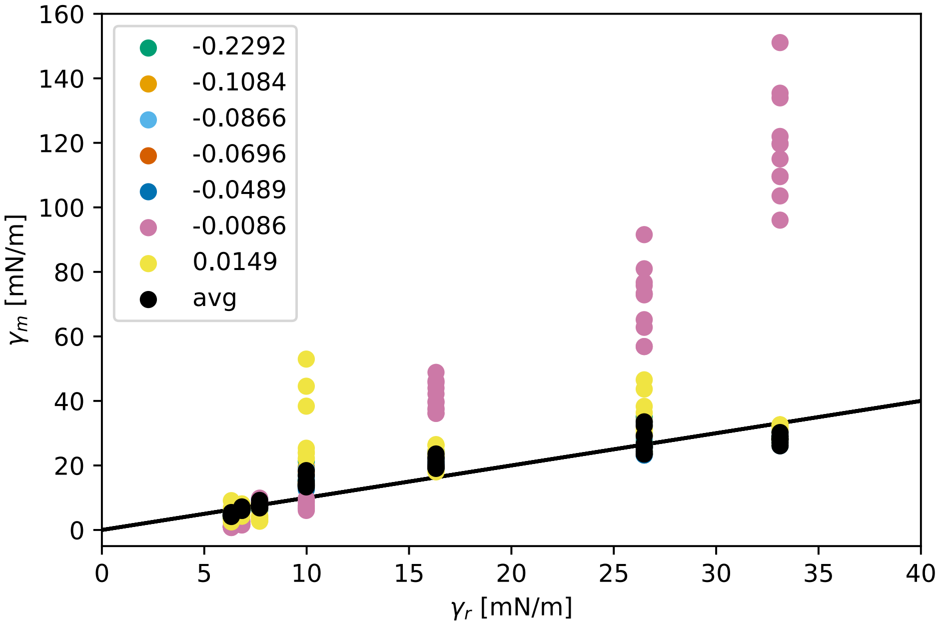

Figure 5.4.4: Parity plot for a range of exponents for Ca. The solid line represent the parity line as a guide for the eye.

It is evident that the outliers observed in Figure 5.4.3 have a large effect on the model. It seems that a positive value of the exponent is not desirable as the deviation from the parity line is large. Further, it seems that for values very close to 0 the deviation from parity is significant. For the remainder of the series, the fit to the parity line is equally good. To better understand the quality of the fit, the R^2-value in relation to the parity line is calculated. The results are shown in Table 5.4.3.

Table 5.4.3: Ca -exponent and the corresponding R^2-value in relation to the parity line.

								Average
Ca^x	-0.2292	-0.1084	-0.0866	-0.0696	-0.0489	-0.0086	0.0149	-0.0766
R^2	0.83	0.85	0.86	0.87	0.89	0.15	0.52	0.87

It is obvious that there are two outliers at the highest values in the Ca exponents. The model has a fit of 0.87 and little improvement can be made by decreasing the exponent.

5.4.3 Summary sensitivity analysis

A sensitivity analysis of the exponents in the model has been carried out. It was found that a value in the lower end of the range for both exponents gives a more accurate model. However, the exponents used in the model give good accuracy and the method of determining the exponents can be defended. It is however important to acknowledge that only the exponents in the model have been investigated in this case. From the collapse of data, a coefficient and constant are also taken into the model. The effect of these parameters has not been investigated as the exponent was deemed to have a larger effect.

5.5 Microfluidic interfacial tension measurements

5.5.1 Static

Figure 5.5.1 show the IFT as a function of surfactant concentration and is analog to Figure 5.1.1 with measurements from the ring tensiometer. The corresponding values from the ring tensiometer are also shown.

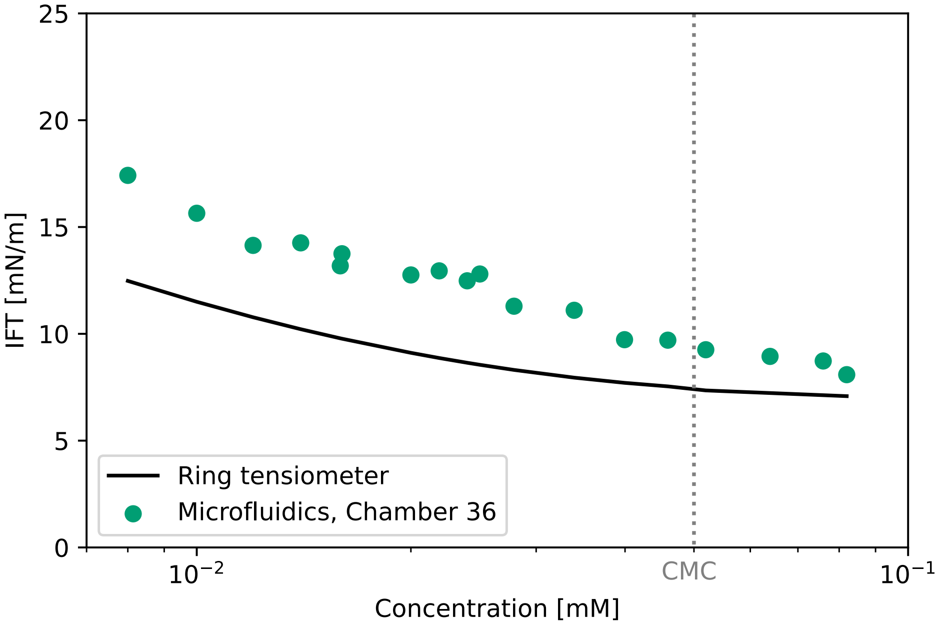

Figure 5.5.1: Static interfacial tension measurement. Results from both microfluidics and ring tensiometer are shown.

The expected trend of decreasing IFT with increasing surfactant concentration can be seen. The IFT measured with the microfluidic method is consistently higher than the ring tensiometer. This suggests that equilibrium is not reached. It is interesting to note that the deviation between the two measurements is slightly higher for lower concentrations than for higher. The model seems to be more accurate at low IFT values, which is in line with what has been discussed earlier.

5.5.2 Dynamic

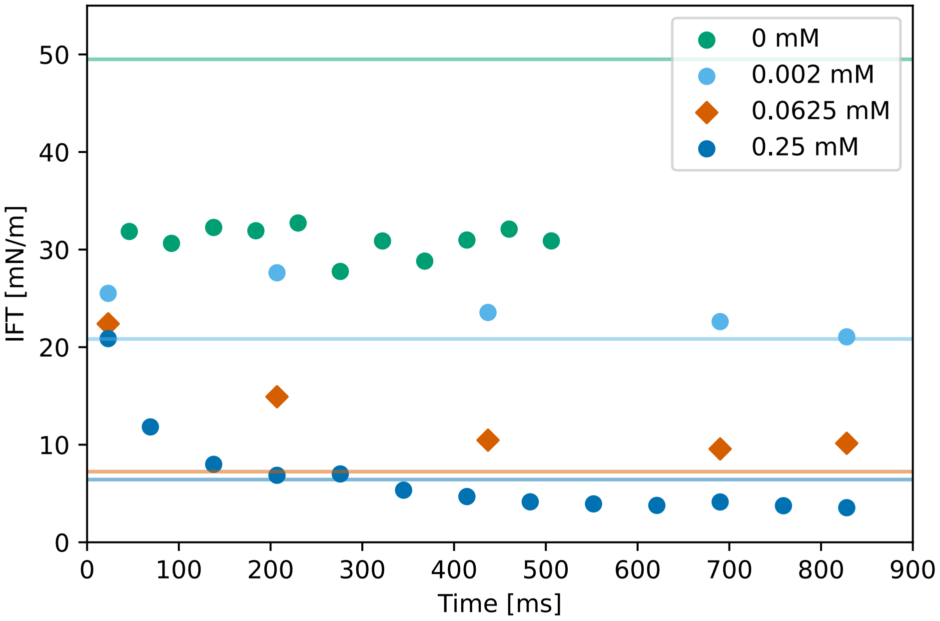

Figure 5.5.2: Dynamic IFT measurements to explore the accuracy of the model for different chip designs.

Diffusion of surfactant to the interface requires time. A decrease in IFT can therefore be observed when recorded over a span of time. Figure 5.5.2 show the IFT as a function of residence time in the chip and is analog to Figure 4.1.1 with measurements from the ring tensiometer. This is achieved by recording the deformation in different chambers across the chip. The equilibrium values from the ring tensiometer are also shown.

It can be seen that some series include more data points than others. This is because only some chambers have been measured for the different series. It can also be seen that for pure water and dodecane the measurements stops after 500 ms, this is because the chip with 22 chambers was used.

The expected trend can be seen for 0.25 and 0.0625 mM. IFT is decreased over time and the final values are close to the expected equilibrium value. For 0.002 mM the trend is not as clear. This suggests that equilibrium is not reached because the concentration of surfactant is small and more time is required than for higher concentrations. For the pure system of water and dodecane, the IFT is relatively stable across the chip. Since no surfactant is present no change in IFT is expected. The value show about 40% deviation from the ring tensiometer. This further confirms that the model is less accurate for high IFTs. The time-scale achieved with microfluidic results is very short. It is possible to look at sub-second timescale, something not feasible with the ring tensiometer. Other measurement techniques may be able to reach similar results. However, the small volumes used also decreases the equilibrium time and offer a unique perspective on dynamic interfacial tension measurements.

5.6 Droplet relaxation

In the project carried out in the fall of 2021 oscillations in aspect ratio as the droplet relaxed into a spherical shape after deformation was observed.[3] Figure 5.6.1 shows the droplet relaxation process for several droplets. The droplet is deformed between x-position 0.4 and 0.45. Afterward, the droplet is relaxed back to a spherical shape, with an aspect ratio of 1. An oscillating trend can be seen as the droplet relaxes.

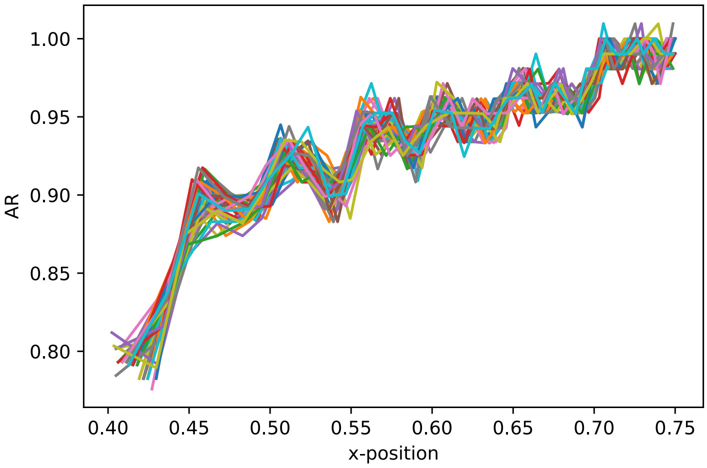

Figure 5.6.1: Droplet relaxation. Several droplets are shown in the same plot and an oscillating relaxation can be seen.

However, when looking at individual droplets the oscillations are less obvious. Figure 5.6.2 shows a few representative droplets. Though it is possible to see trends in the plots, it appears more sporadic and less structured.

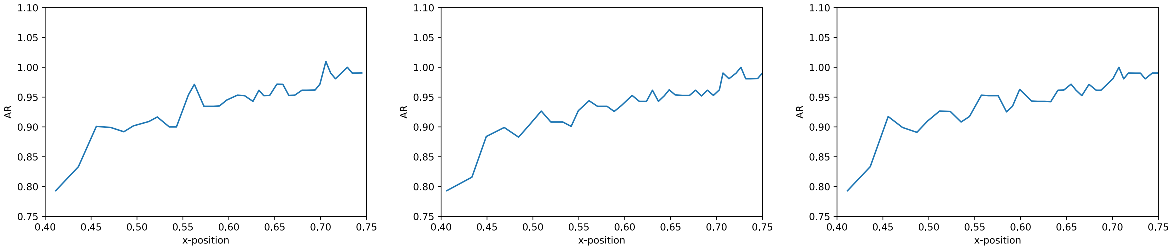

Figure 5.6.2: Examples of droplet relaxation for single droplets.

To investigate this behavior further recordings of droplets were made at a higher frame rate (12 000 fps) with the aim of capturing the oscillations more clearly. Figure 5.6.3 shows the results. The figure to the left show single droplets, while the right figure show a scatter plot of all the data.

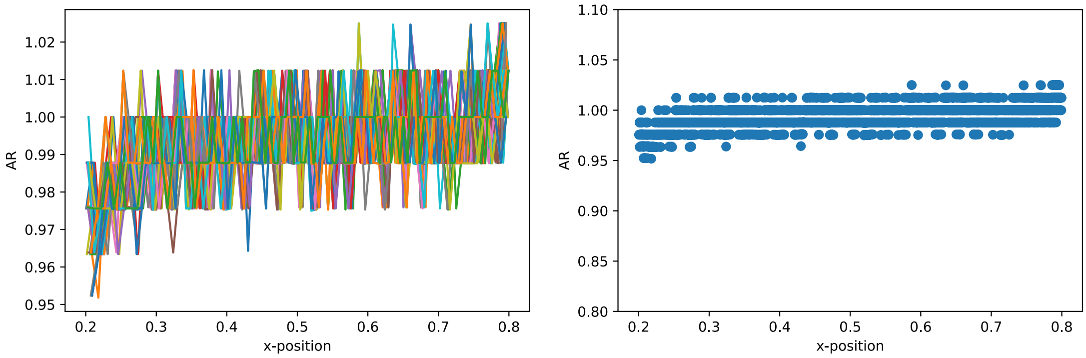

Figure 5.6.3: Aspect ratio plotted against x-position for recordings made at a higher frame rate. The left figure shows single droplets while the figure to the right show all the data.

It can be seen that the trend observed earlier cannot be seen when the frame rate is increased. From the figure on the right, there seems to be some sort of discrete distribution of the data. This may be explained by the nature of the aspect ratio. The aspect ratio is a fraction where both the numerator and the denominator are whole numbers. This stem from the fact that the image analysis returns pixel values for the positions and dimensions measured. It is therefore believed that the oscillations seen, stems from the fact that the bounding box is placed on the pixel grid and may cause results resembling oscillations. The oscillations may therefore be an artifact caused by the lower limit to the measurement magnitude. This limitation is traced back to the camera resolution and the magnification by the camera objective.

Another possible explanation is that when the neural network detects droplets and draws the bounding box there are some inaccuracies. If the box moves relative to the droplet this may explain the reason for the oscillations in aspect ratio being seen for all droplets and not for the single droplets. This may also be further caused by the focus of the camera. The thickness of the chip is 45 µm which means that the droplets have a pancake shape, rather than a spherical shape. If the chip is tilted enough to give a variation in the focus plane, the droplet will change size. However, since the distances in question are very small this is not believed to be a major concern.

When a droplet is deformed by a force and the force is removed the droplet will return to a spherical shape. This relaxation is expected to have a dampening trend. Although there is reason to believe that the oscillations seen are artifacts this has not been proven. The oscillations may be too fast or too small to be observed in the experiments made in this work. The oscillations may also be lost in the image analysis, so using an alternative analysis (f.ex. Image J) with better accuracy may resolve this. Due to time constraints, this has not been explored further in this thesis but is recommended as further work in this field.

Chapter 6

Conclusion and further work

6.1 Conclusion

A microfluidic model for interfacial tension measurements has been developed. The model was fitted to experimental data for a range of values of IFT and measurements from the ring tensiometer were used as a reference. The model validity has been tested by examining the effect of both velocity and chip design. It was found that the model is accurate within the IFT and velocity range used to fit the model. However, at high IFTs the model loses accuracy. Potential errors which may propagate into the model have been discussed and measures have been implemented to reduce the error in the final model.

The microfluidic tensiometer shows promising improvements when compared to a traditional tensiometer. The measurement time is reduced significantly, and the flexibility the instrument offers is a large improvement. The sample size has been reduced tenfold, compared to the ring tensiometer, an important improvement for biological applications where the sample may be limited. However, work still remains before the method can be widely used. Most important, at this stage, a traditional tensiometer is still required to fit the model. The accuracy of the model has not been determined numerically, which is important for any application of the method.

6.2 Further work

The chip design was identified as one of the limiting factors in this thesis. The exploration of diverse chip designs would increase the control of droplets and velocity. One interesting design includes the introduction of surfactant mid-chip to have a reference state where no surfactant is present. Increasing the retention time in the chip to ensure equilibrium can be observed would be beneficial for dynamic IFT measurements. The size and geometry of chambers should be explored to understand the effect on the model.

The model development presented here can be explored further to better understand the effect of the fitting parameters on the measurement. Work should also be made to derive a physical relationship between the interfacial tension and the deformation. This may result in a more robust and universal model. The work on droplet relaxation presented in this work may be expanded to understand if the elasticity is also a property one can measure using microfluidics.

Finally, other surfactants and oils should be explored. Both variations in charge and solubility of the surfactant should be examined to better understand the possibilities and limitations of microfluidic interfacial tension measurements.

Bibliography

[1] P.C. Mørk. *Surface and colloid chemistry. Basic principles and theories.* Department of Chemical Engineering, 2004.

[2] D. Shaw and D.J. Shaw. *Introduction to Colloid and Surface Chemistry.* Elsevier Science, 4th edition, 1992.

[3] V.M. Selvik. Microfluidic interfacial tension: Specialization project. Specialization project at Ugelstad Laboratories, fall 2021, 2021.

[4] Quentin Brosseau, Jérémy Vrignon, and J. C. Baret. Microfluidic dynamic interfacial tensiometry (μdit). *Soft matter*, 2014.

[5] Jaroslaw Drelich, Ch Fang, and Calvin White. *Measurement of interfacial tension in Fluid-Fluid Systems*, pages 3152–3166. Marcel Dekker Inc., 01 2002.

[6] G.M. Kontogeorgis and S. Kiil. *Introduction to Applied Colloid and Surface Chemistry.* Wiley, 2016.

[7] Drew Mayers. *Surfactant Science and Technology.* John Wiley and Sons, Ltd, 2005.

[8] Clarence Miller and P. Neogi. *Interfacial phenomena.* CRC press, 2008.

[9] G. Barnes and I. Gentle. *Interfacial Science: An Introduction.* Oxford University Press, 2005.

[10] Milton J. Rosen and Joy T. Kunjappu. *Surfactants and Interfacial Phenomena.* John Wiley and Sons, Ltd, 2012.

[11] Sigma-Aldrich. Tween 20 CAS NO.9005-64-5, 2022. URL `https://www.sigmaaldrich.com/NO/en/product/sial/p1379`.

[12] George M. Whitesides. The origins and the future of microfluidics. *Nature*, 442, 2006.

[13] Tharwat Tadros. *Emulsion Formation and Stability.* Wiley-VCH, 2013.

[14] Marcin J. Dudek. *Produced Water Quality and Microfluidic Methods for Studying Drop-Drop and Drop-Bubble Interactions in Produced Water.* PhD thesis, Norwegian University of Science and Technology, 2018.

[15] Karin Schroën, Jolet de Ruiter, and Claire Berton-Carabin. The importance of interfacial tension in emulsification: Connecting scaling relations used in large scale preparation with microfluidic measurement methods. *ChemEngineering*, 2020.

[16] João T. Cabral and Steven D. Hudson. Microfluidic approach for rapid multicomponent interfacial tensiometry. *Lab on a Chip*, 2006.

[17] Lingling Kong, Kadi Liis Saar, Raphael Jacquat, Liu Hong, Aviad Levin, Hongze Gang, Ruqiang Ye, Bozhong Mu, and Tuomas P. J. Knowles. Mechanism of biosurfactant adsorption to oil/water interfaces from millisecond scale tensiometry measurements. *Interface Focus*, 2017.

[18] Estelle André, Nicolas Pannacci, Christine Dalmazzone, and Annie Colin. A new way to measure viscosity in droplet-based microfluidics for high throughput analysis. *Soft Matter*, 2019.

[19] Arthur W. Adamson and Alice P. Gast. *Physical Chemistry of Surfaces.* Wiley, 1997.

[20] Sina Ebnesajjad and Arthur H. Landrock. Chapter 2 - surface tension and its measurement. In Sina Ebnesajjad and Arthur H. Landrock, editors, *Adhesives Technology Handbook (Third Edition)*, pages 19–34. William Andrew Publishing, third edition, 2015.

[21] iGEM 2019: Tec-monterrey, hardware, 2019. URL `https://2019.igem.org/Team:Tec-Monterrey/Hardware`.

[22] Piotr Garstecki. Formation of bubbles and droplets in microfluidic systems. *Bulletin of the Polish Academy of Sciences, Technical Sciences*, 53, 2005.

[23] Pingan Zhu and Liqiu Wang. Passive and active droplet generation with microfluidics: a review. *Lab on a Chip*, 17, 2017.

[24] Corentin Tregouet, Thomas Salez, Cécile Monteux, and Mathilde Reyssat. Transient deformation of a droplet near a microfluidic constriction: A quantitative analysis. *Physical Review Fluids*, 3, 01 2018.

[25] Joseph Redmon, Santosh Divvala, Ross Girshick, and Ali Farhadi. You only look once: Unified, real-time object detection. In *Proceedings of the IEEE Conference on Computer Vision and Pattern Recognition (CVPR)*, June 2016.

[26] Gregory Philip Rutkowski, Ilgar Azizov, Evan Unmann, Marcin Dudek, and Brian Arthur Grimes. Microfluidic droplet detection via region-based and single-pass convolutional neural networks with comparison to conventional image analysis methodologies. *Machine Learning with Applications*, 2022.

[27] Gonzalo Vázquez, Estrella Alvarez, and José M. Navaza. Surface tension of alcohol + water from 20 to 50 ℃. *Chem. Eng. Data*, 1995.

[28] Katarzyna Szymczyk, Magdalena Szaniawska, and Anna Taraba. Micellar parameters of aqueous solutions of tween 20 and 60 at different temperatures: Volumetric and viscometric study. *Colloids and Interfaces*, 2018.

Appendix A

Experimental work

A.1 Experimental matrix

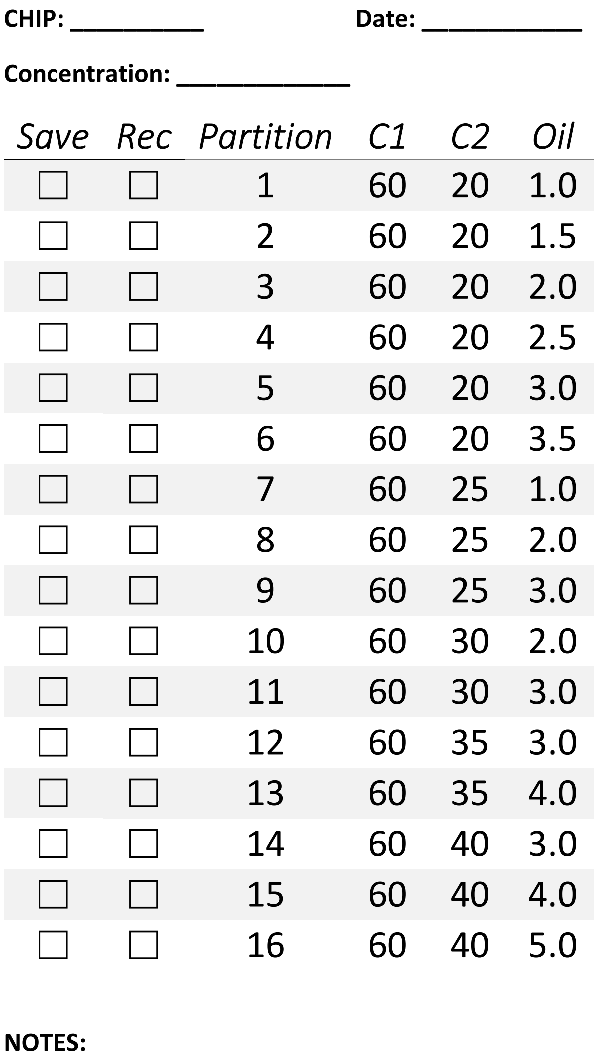

CHIP: __________ **Date:** ____________

Concentration: _____________

Save	*Rec*	*Partition*	*C1*	*C2*	*Oil*
☐	☐	1	60	20	1.0
☐	☐	2	60	20	1.5
☐	☐	3	60	20	2.0
☐	☐	4	60	20	2.5
☐	☐	5	60	20	3.0
☐	☐	6	60	20	3.5
☐	☐	7	60	25	1.0
☐	☐	8	60	25	2.0
☐	☐	9	60	25	3.0
☐	☐	10	60	30	2.0
☐	☐	11	60	30	3.0
☐	☐	12	60	35	3.0
☐	☐	13	60	35	4.0
☐	☐	14	60	40	3.0
☐	☐	15	60	40	4.0
☐	☐	16	60	40	5.0

NOTES:

Figure A.1.1: Experimental matrix for the experiments outlined in Section 5.2. The flow rates on the different syringes are given in µL/min. LP1 is the syringe controlling the flow of C1, LP2 control C2 and LP5 is the oil phase flow.

The concentrations/IFT values used in the 7 experiments to fit the model can be found in Table A.1.1. The corresponding IFT values from the ring tensiometer is also given.

Table A.1.1: Concentrations with the corresponding measured IFT used to fit the model.

Concentration	0.0005	0.001	0.0039	0.015	0.125	0.04	0.3	[mM]
IFT	33.12	26.49	16.32	9.98	7.70	6.8	6.32	[mN/m]

Appendix B

Supplementary material

B.1 Linear regression for model fitting

To determine the exponents of R* and Ca in the model, linear regression on a log-log plot of AR against the respective variables were made. In this case, the exponent of the variable is analog to the slope. The exponent used in the model is an average of the fits. Figure B.1.1 show the regressions with the corresponding R^2 value in the legend. The black line represents the average and chosen exponent.

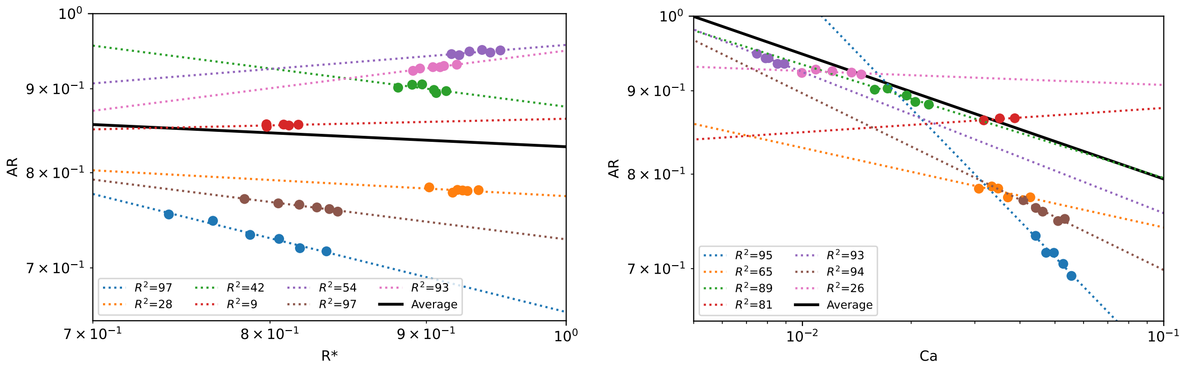

(a) Constant velocity.

(b) Constant size

Figure B.1.1: Linear regression to determine exponent. An average of the exponents for all regression is used in the final model and is shown as the black line in the plots. The R^2-value for each regression is given in the legend. The black line shows the average slope used in the model.

B.2 Error analysis

Plots from Section 5.2.3 is here presented with the uncertainties related to the parameters. The error in AR is given as the standard deviation calculated from all droplets in the same experiment. R^* is defined as the diameter divided by a given length chosen to be the width of the channel, $R^* = 2R/W$. The error in R^* is calculated using the weighted sum of the errors of each parameters by a method names Gauss error propagation.

$$s_{R^*}^2 = \left(\frac{\partial R^*}{\partial D}\right)^2 s_D^2 + \left(\frac{\partial R^*}{\partial W}\right)^2 s_W^2 \tag{B.2.1}$$

Where s_i is the error in variable i. W is equal to 10^{-4} µm and assumed to have no error. The second term can therefore be neglected. The final expression of the error is then

$$s_{R^*} = \sqrt{\left(\frac{1}{10^{-4}}\right)^2 s_D^2} \tag{B.2.2}$$

Figure B.2.1 show AR as a function of R* with error bars included.

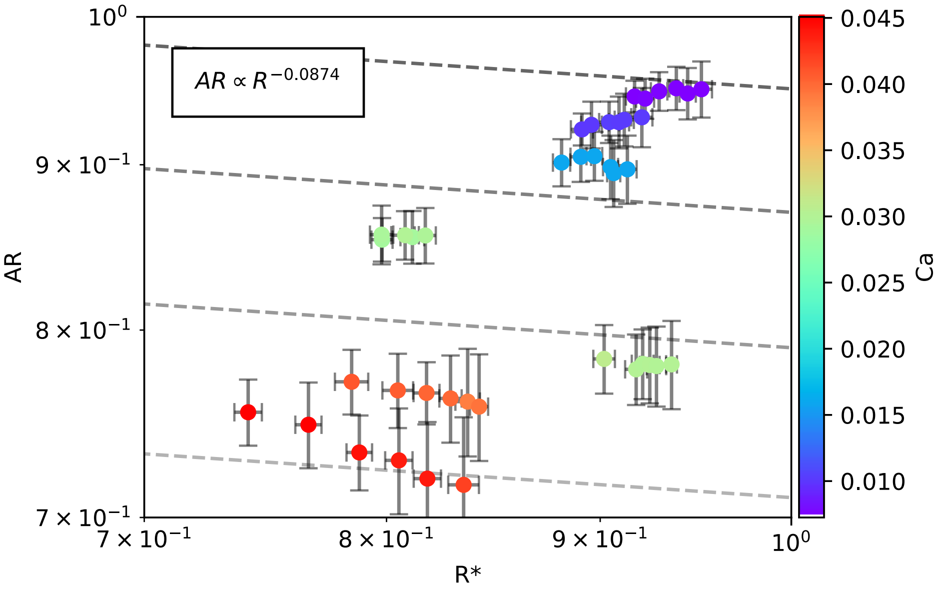

Figure B.2.1: Plot for constant velocity presented in Figure 5.2.5 shown with error bars in both AR and R*.

Ca is defined as $Ca = \eta U/\gamma$.The error is given by Equation B.2.3.

$$s_{Ca}^2 = \left(\frac{\partial Ca}{\partial \eta}\right)^2 s_\eta^2 + \left(\frac{\partial Ca}{\partial U}\right)^2 s_U^2 + \left(\frac{\partial Ca}{\partial \gamma}\right)^2 s_\gamma^2 \tag{B.2.3}$$

The viscosity is assumed constant and with no error. γ is the interfacial tension retrieved from the ring tensiometer results. To determine s_γ one must take into consideration both the error inherent to the measurement and errors propagated through the regression made. This quickly becomes quite complicated and is therefore not included in this thesis. Figure B.2.2 show AR as a function of Ca with error bars on in the AR values.

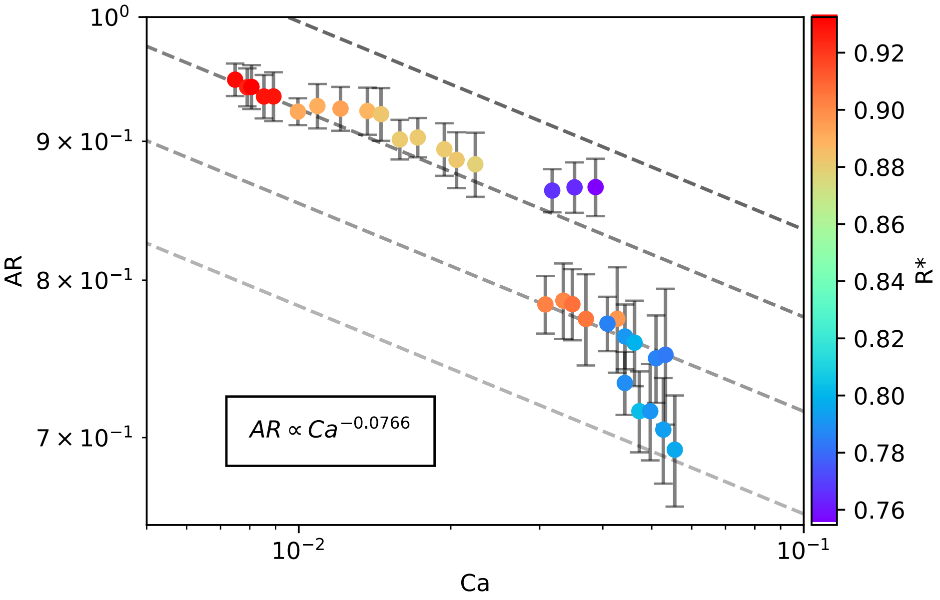

Figure B.2.2: Plot for constant size presented in Figure 5.2.6 shown with error bars for AR.

The collapse of the data with error bars for AR is shown in Figure B.2.3.

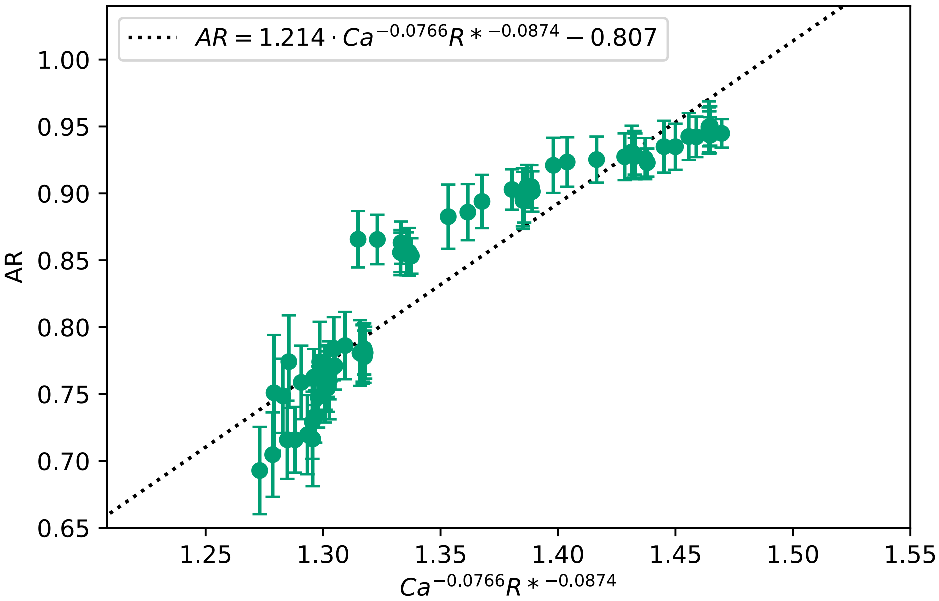

Figure B.2.3: The collapse of data with error bars.

The model developed in this thesis presents the interfacial tension as a function of viscosity, velocity, diameter, and deformation: $\gamma(\eta, U, D, AR)$. Each of these parameters in themselves contains a certain uncertainty. The error is calculated using Gauss Error propagation as shown in Equation B.2.4.

$$s_\gamma^2 = \left(\frac{\partial \gamma}{\partial \eta}\right)^2 s_\eta^2 + \left(\frac{\partial \gamma}{\partial U}\right)^2 s_U^2 + \left(\frac{\partial \gamma}{\partial D}\right)^2 s_D^2 + \left(\frac{\partial \gamma}{\partial AR}\right)^2 s_{AR}^2 \tag{B.2.4}$$

where s_i is the error of parameter i, and γ is equal to Equation 5.2.1. Viscosity is assumed to have no error. The derivatives can be seen below. For simplicity the exponents are abbreviated as $a = -\frac{1}{0.0766}$ and $b = -0.0874$

$$\frac{\partial \gamma}{\partial U} = \eta \left(1.73 \cdot D^b\right)^a \left(\frac{1}{AR + 0.73}\right)^a \tag{B.2.5}$$

$$\frac{\partial \gamma}{\partial D} = a \cdot b \cdot \eta \cdot U \cdot 1.73^a \left(\frac{1}{AR + 0.73}\right)^a D^{ab-1} \tag{B.2.6}$$

$$\frac{\partial \gamma}{\partial AR} = -a \cdot \eta \cdot U \left(1.73 \cdot D^b\right)^a \left(\frac{1}{AR + 0.73}\right)^{a+1} \tag{B.2.7}$$

$$\tag{B.2.8}$$

Figure B.2.4 show the parity plot with error bars.

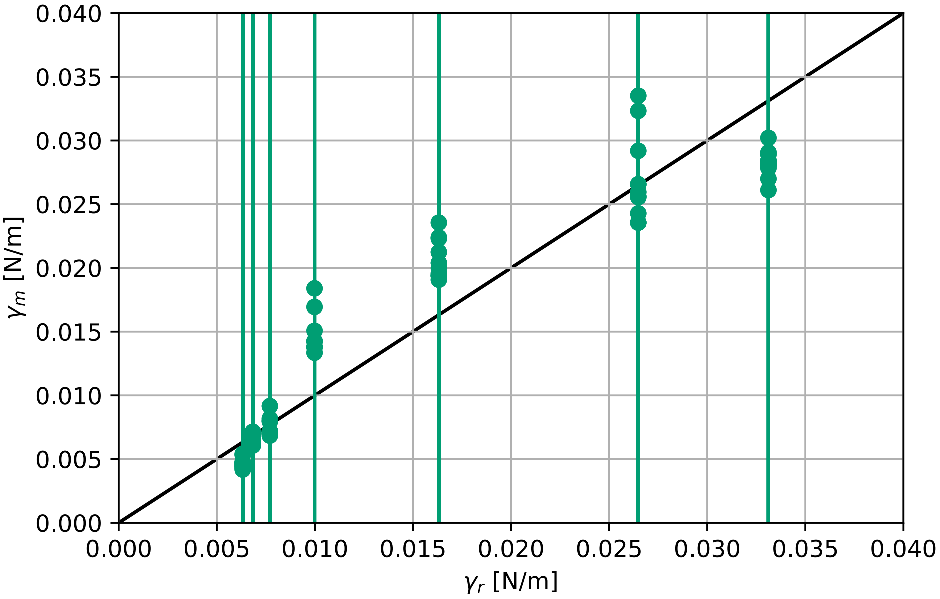

Figure B.2.4: Parity plot between the microfluidic model and the ring tensiometer results with error bars.

It can be seen that the error is very large. It has been found that the deformation has a larger effect on the error value. It is believed that calculating the error using another method would give more reasonable errors. However, due to time constraints this is not in the scope of this thesis.

Appendix C

Raw data

Conc.	**C1**	**C2**	**Oil**	**Total**	**Velocity**		s_U	**AR**		s_{AR}	**D**		s_D	**Drops**	R*	Ca
[mM]		[µL/min]			[m/s]			[-]			[m]			[-]	[-]	[-]
0.3	60	20	2	80	0.280	±	0.020	0.73	±	0.02	7.88E-05	±	5.55E-07	126	0.788	0.044
0.3	60	25	3	85	0.299	±	0.027	0.72	±	0.02	8.02E-05	±	4.17E-07	201	0.802	0.047
0.3	60	30	3	90	0.314	±	0.028	0.72	±	0.03	7.91E-05	±	5.33E-07	214	0.791	0.050
0.3	60	35	4	95	0.333	±	0.030	0.70	±	0.03	7.93E-05	±	4.47E-07	276	0.793	0.053
0.3	60	40	5	100	0.351	±	0.035	0.69	±	0.03	7.96E-05	±	5.66E-07	358	0.796	0.056
0.3	60	20	1.5	80	0.285	±	0.023	0.75	±	0.02	7.66E-05	±	5.53E-07	87	0.766	0.045
0.3	60	20	1	80	0.284	±	0.022	0.75	±	0.02	7.41E-05	±	5.62E-07	39	0.741	0.045
0.3	60	20	2.5	80	0.276	±	0.027	0.73	±	0.03	8.05E-05	±	6.08E-07	157	0.805	0.044
0.3	60	20	2	80	0.280	±	0.020	0.73	±	0.02	7.88E-05	±	5.55E-07	126	0.788	0.044
0.3	60	20	3.5	80	0.265	±	0.031	0.72	±	0.04	8.35E-05	±	7.07E-07	212	0.835	0.042
0.3	60	20	3	80	0.277	±	0.026	0.72	±	0.03	8.18E-05	±	6.15E-07	189	0.818	0.044
0.04	60	20	1	80	0.237	±	0.028	0.78	±	0.02	9.02E-05	±	5.37E-07	51	0.902	0.031
0.04	60	25	2	85	0.257	±	0.029	0.79	±	0.03	9.01E-05	±	5.82E-07	111	0.901	0.033
0.04	60	30	3	90	0.268	±	0.035	0.78	±	0.02	9.06E-05	±	4.81E-07	173	0.906	0.035
0.04	60	35	4	95	0.285	±	0.035	0.77	±	0.03	9.05E-05	±	5.42E-07	232	0.905	0.037
0.04	60	40	5	100	0.329	±	0.031	0.77	±	0.03	8.97E-05	±	2.02E-07	290	0.897	0.043
0.04	60	20	1	80	0.237	±	0.028	0.78	±	0.02	9.02E-05	±	5.37E-07	51	0.902	0.031

0.04	60	20	1.5	80	0.232	±	0.029	0.78	±	0.02	9.18E-05	±	5.58E-07	84	0.918	0.030
0.04	60	20	2	80	0.231	±	0.034	0.78	±	0.02	9.21E-05	±	5.53E-07	107	0.921	0.030
0.04	60	20	2.5	80	0.232	±	0.030	0.78	±	0.02	9.25E-05	±	5.04E-07	132	0.925	0.030
0.04	60	20	3	80	0.231	±	0.031	0.78	±	0.02	9.28E-05	±	4.98E-07	154	0.928	0.030
0.04	60	20	3.5	80	0.231	±	0.033	0.78	±	0.02	9.36E-05	±	2.80E-07	182	0.936	0.030
0.0039	60	20	1	80	0.259	±	0.027	0.90	±	0.02	8.81E-05	±	4.20E-07	59	0.881	0.016
0.0039	60	25	2	85	0.281	±	0.028	0.90	±	0.02	8.80E-05	±	4.27E-07	121	0.880	0.017
0.0039	60	30	3	90	0.317	±	0.026	0.89	±	0.02	8.81E-05	±	5.33E-07	184	0.881	0.019
0.0039	60	35	4	95	0.335	±	0.028	0.89	±	0.02	8.82E-05	±	5.51E-07	244	0.882	0.021
0.0039	60	40	5	100	0.365	±	0.030	0.88	±	0.02	8.78E-05	±	1.57E-07	313	0.878	0.022
0.0039	60	20	1	80	0.259	±	0.027	0.90	±	0.02	8.81E-05	±	4.20E-07	59	0.881	0.016
0.0039	60	20	1.5	80	0.257	±	0.028	0.91	±	0.02	8.90E-05	±	5.06E-07	93	0.890	0.016
0.0039	60	20	2	80	0.259	±	0.029	0.91	±	0.02	8.97E-05	±	3.89E-07	119	0.897	0.016
0.0039	60	20	2.5	80	0.259	±	0.027	0.90	±	0.02	9.05E-05	±	3.76E-07	150	0.905	0.016
0.0039	60	20	3	80	0.260	±	0.028	0.89	±	0.02	9.07E-05	±	3.28E-07	170	0.907	0.016
0.0039	60	20	3.5	80	0.258	±	0.030	0.90	±	0.02	9.14E-05	±	4.67E-07	195	0.914	0.016
0.015	60	25	1	85	0.317	±	0.027	0.86	±	0.02	7.66E-05	±	5.81E-07	79	0.766	0.032
0.015	60	30	2	90	0.351	±	0.026	0.87	±	0.02	7.64E-05	±	5.06E-07	166	0.764	0.035
0.015	60	35	3	95	0.386	±	0.024	0.87	±	0.02	7.55E-05	±	6.47E-07	260	0.755	0.039
0.015	60	20	1	80	0.290	±	0.025	0.85	±	0.01	7.98E-05	±	4.65E-07	77	0.798	0.029
0.015	60	20	1.5	80	0.293	±	0.024	0.86	±	0.02	7.98E-05	±	5.15E-07	100	0.798	0.029
0.015	60	20	2	80	0.290	±	0.025	0.85	±	0.02	8.11E-05	±	5.31E-07	150	0.811	0.029
0.015	60	20	2.5	80	0.299	±	0.026	0.86	±	0.01	8.08E-05	±	6.14E-07	165	0.808	0.030
0.015	60	20	3	80	0.295	±	0.027	0.86	±	0.02	8.17E-05	±	4.75E-07	213	0.817	0.030
0.0005	60	20	2	80	0.248	±	0.023	0.95	±	0.01	9.30E-05	±	4.22E-07	103	0.930	0.007
0.0005	60	25	2	85	0.262	±	0.025	0.94	±	0.02	9.25E-05	±	4.25E-07	107	0.925	0.008
0.0005	60	30	3	90	0.267	±	0.028	0.94	±	0.02	9.32E-05	±	4.53E-07	155	0.932	0.008
0.0005	60	35	3	95	0.283	±	0.025	0.93	±	0.02	9.28E-05	±	4.99E-07	168	0.928	0.009
0.0005	60	40	4	100	0.295	±	0.027	0.93	±	0.02	9.28E-05	±	4.68E-07	209	0.928	0.009
0.0005	60	20	1	80	0.240	±	0.026	0.94	±	0.01	9.17E-05	±	4.37E-07	51	0.917	0.007
0.0005	60	20	1.5	80	0.249	±	0.023	0.94	±	0.01	9.23E-05	±	4.56E-07	77	0.923	0.008
0.0005	60	20	2	80	0.248	±	0.023	0.95	±	0.01	9.30E-05	±	4.22E-07	103	0.930	0.007
0.0005	60	20	2.5	80	0.244	±	0.021	0.95	±	0.01	9.39E-05	±	3.57E-07	131	0.939	0.007
0.0005	60	20	3	80	0.244	±	0.022	0.95	±	0.02	9.44E-05	±	4.23E-07	152	0.944	0.007
0.0005	60	20	3.5	80	0.242	±	0.020	0.95	±	0.02	9.52E-05	±	5.58E-07	171	0.952	0.007

0.125	60	20	1	80	0.279	±	0.023	0.77	±	0.02	7.85E-05	±	7.21E-07	62	0.785	0.041
0.125	60	25	2	85	0.303	±	0.022	0.76	±	0.02	7.91E-05	±	7.03E-07	140	0.791	0.044
0.125	60	30	3	90	0.316	±	0.027	0.76	±	0.03	7.99E-05	±	5.26E-07	224	0.799	0.046
0.125	60	35	4	95	0.349	±	0.027	0.75	±	0.03	7.86E-05	±	5.68E-07	305	0.786	0.051
0.125	60	40	5	100	0.364	±	0.032	0.75	±	0.04	7.83E-05	±	4.79E-07	383	0.783	0.053
0.125	60	20	1	80	0.279	±	0.023	0.77	±	0.02	7.85E-05	±	7.21E-07	62	0.785	0.041
0.125	60	20	1.5	80	0.278	±	0.023	0.77	±	0.02	8.05E-05	±	6.82E-07	105	0.805	0.041
0.125	60	20	2	80	0.275	±	0.024	0.76	±	0.02	8.18E-05	±	5.85E-07	137	0.818	0.040
0.125	60	20	2.5	80	0.273	±	0.027	0.76	±	0.02	8.29E-05	±	5.09E-07	183	0.829	0.040
0.125	60	20	3	80	0.266	±	0.030	0.76	±	0.03	8.37E-05	±	5.65E-07	198	0.837	0.039
0.125	60	20	3.5	80	0.269	±	0.031	0.76	±	0.03	8.42E-05	±	4.21E-07	233	0.842	0.039
0.001	60	20	1	80	0.264	±	0.025	0.92	±	0.01	8.91E-05	±	5.43E-07	43	0.891	0.010
0.001	60	25	2	85	0.288	±	0.027	0.93	±	0.02	8.89E-05	±	5.24E-07	110	0.889	0.011
0.001	60	30	3	90	0.320	±	0.024	0.93	±	0.02	8.93E-05	±	4.86E-07	168	0.893	0.012
0.001	60	35	4	95	0.362	±	0.023	0.92	±	0.02	8.88E-05	±	5.36E-07	224	0.888	0.014
0.001	60	40	5	100	0.385	±	0.026	0.92	±	0.02	8.82E-05	±	4.63E-07	288	0.882	0.015
0.001	60	20	1	80	0.264	±	0.025	0.92	±	0.01	8.91E-05	±	5.43E-07	43	0.891	0.010
0.001	60	20	1.5	80	0.264	±	0.025	0.93	±	0.02	8.96E-05	±	5.13E-07	71	0.896	0.010
0.001	60	20	2	80	0.272	±	0.022	0.93	±	0.01	9.04E-05	±	4.98E-07	103	0.904	0.010
0.001	60	20	2.5	80	0.270	±	0.025	0.93	±	0.02	9.09E-05	±	5.06E-07	125	0.909	0.010
0.001	60	20	3	80	0.270	±	0.029	0.93	±	0.02	9.12E-05	±	4.82E-07	148	0.912	0.010
0.001	60	20	3.5	80	0.270	±	0.026	0.93	±	0.02	9.21E-05	±	5.38E-07	180	0.921	0.010

Appendix D

Scripts

```python
# -*- coding: utf-8 -*-
"""
Created on Mon Apr  4 15:30:57 2022

@author: Veslemoy Selvik
"""
"""--------------------- Utilities -----------------------------------------"""

import pandas as pd
from matplotlib import pyplot as plt
import numpy as np
import statistics as s
import re
import time
import os
import sys
import inspect
from scipy.optimize import curve_fit
def sigmoid(x, a, L, x0, k):
    y = a+L/(1 + np.exp(k*(x-x0)))
    return y


"""------------------------- Input -----------------------------------------"""
paths = []
path_i = r'D:\Spring22\Model_Development\2022-03-30_TW20_0.3mM_FF36C'
paths.append(path_i)

for path_i in paths:

    # path = path_i + '\Const_Size\chosen'
    path = path_i + '\Const_Velocity'

    eta = 0.001 # Pa s (= 1 mPa s)

    """------------------------- Define variables
    -----------------------------------------"""
    dirlist = []
    # Make list of paths to 'bottom' folder
    for root, d_names, f_names in os.walk(path):
        if not d_names:
            dirlist.append(root)
    print('Number of files:', len(dirlist))
    # end_script = input('Continue?(y/n)')
    end_script = 'y'
    # if end_script == 'n':
    #     print('Script terminated.')
    #     sys.exit()
    # save = input('Save data?(y/n)')
    save = 'y'

```

```


    # Make lists to fill
    conc = []
    LP1 = []
    LP2 = []
    LP5 = []
    TotFlow = []
    V = []
    VSD = []
    AR = []
    SD = []
    D = []
    DSD = []
    droplets = []
    R = []
    Ca = []

    counter = 1
    counter_tot = len(dirlist)
    start_time = time.time()

    for d in dirlist:
        t0 = time.time()
        """--------------------- Concentration ---------------------------------"""
        # Concentration is found from folder names by finding the index of ’mM’
        # and going   backwards until there is a ’_’. This is specific to the
        # naming convention chosen. Needed for IFT calculations.

        i = d.find(’mM’)
        for l in range(i, 0, -1):
            if d[l] == ’_’:
                j = l+1
                break
        C = float(d[j:i])
        conc.append(C)

        """--------------------- IFT ---------------------------------"""
        # IFT is determined based on the ring tensiometer results. Two fits has
        # been made. One above and one below CMC. Based on the concentration found
        # previously the IFT can be calculated. Needed for Ca calculations.
        # IFT in N/m
        if C >= 0.05: # Above CMC
            IFT = (-1.35034 * np.log10(C) + 5.61615)/1000
        elif C < 0.05: # Below CMC
            IFT = (5.41983 * np.log10(C)**2 + 12.1122 * np.log10(C) + 14.0443 )/1000
        else:
            IFT = -1
            print(’\t\tError line’, inspect.currentframe().f_lineno, ’: IFT not found’)


        """--------------------- Flows -----------------------------------------"""
        # The flows are found by determining all indexes where ’_’ occur. By the
        # naming convention chosen the flows are separated by an underscore and
        # the order is known.
        # Not needed, but used to identify experiments with the same cont. flow.

        result = [_.start() for _ in re.finditer(’_’, d)]  # Find indexes of _

        LP1_temp = float(d[result[-4]+1:result[-3]])
        LP2_temp = float(d[result[-3]+1:result[-2]])
        LP5_temp = float(d[result[-2]+1:result[-1]])
        TotFlow_temp = LP1_temp + LP2_temp

        LP1.append(LP1_temp)
        LP2.append(LP2_temp)
        LP5.append(LP5_temp)
        TotFlow.append(TotFlow_temp)

        """------------------------ CSV to df ----------------------------------"""
        # Read the CSV into a DataFrame to be manipulated later.

        output = d + ’\organized.csv’
```

```
        df = pd.read_csv(output, header=0, delimiter=',')
        # Headers: Unnamed, Droplet_ID, Frame
        # X , Y  - Position of center
        # X1, Y1 - Position of upper left corner
        # X2, Y2 - Position of lower right corner

        """----------------------- Formatting ----------------------------------"""
        # Remove droplets on edge. Pixels used here.

        df = df.drop(df[df.X1 <= 5.0].index)
        df = df.drop(df[df.X2 >= 380.0].index)

        """----------------------- Pixel to micrometer -------------------------"""
        # Transform to meter.
        # x[m] = x[-]* micrometer/pixel(0.97, found using PFV/ImageJ) * 10^-6 m/um

        df.X *= 0.97*10**(-6)
        df.Y *= 0.97*10**(-6)
        df.D *= 0.97*10**(-6)
        df.X1 *= 0.97*10**(-6)
        df.Y1 *= 0.97*10**(-6)
        df.X2 *= 0.97*10**(-6)
        df.Y2 *= 0.97*10**(-6)

        """------------------------ df to lists --------------------------------"""
        # Make lists from df (for calculation of AR)

        X1 = df['X1'].tolist()
        X2 = df['X2'].tolist()
        Y1 = df['Y1'].tolist()
        Y2 = df['Y2'].tolist()

        """--------------------- calculations ----------------------------------"""
        # Calculate AR elementwise
        AR_calc = [((x2-x1)/(y2-y1)) for x1, x2, y1, y2 in zip(X1, X2, Y1, Y2)]
        H = [(y2-y1) for y1, y2 in zip(Y1, Y2)]
        W = [(x2-x1) for x1, x2 in zip(X1, X2)]

        # Add AR column to df
        df['AR'] = AR_calc
        df['Height'] = H
        df['Width'] = W

        """--------------------- Re-label duplicate indices --------------------"""
        # Some droplets have the same indexes. To fix this the change in
        # x position is checked for ech droplet. If (Xi-X(i-1)) is negative a new
        # droplet is detected and a new index should be added.

        dropletID = [] # List to be filled with current droplet IDs
        [dropletID.append(x) for x in df['Droplet_ID'] if x not in dropletID]

        for i in dropletID:  # For all droplet IDs
            # Extract only droplets with ID = i
            drop = df.loc[df['Droplet_ID'] == i]
            last = drop.index[-1]
            diff = drop.diff()  # Last row (i-1) minus current row (i)
            diff.dropna() # Remove NaNs

            neg = diff.index[diff['X'] < 0.0].tolist() # indexes where diff is negative
            neg.append(last)
            for i in range(len(neg)-1):
                newID = max(df['Droplet_ID'])+1 # Add new index after the max
                df.loc[neg[i]:neg[i+1], 'Droplet_ID'] = newID # Set new ID


        """-------------------- Remove "non-monodisperse" droplets -------------"""
        # Some droplets were observed to be sligtly larger than the mean. This is
        # thought to be mostly due to the accuracy of the detecion of droplets.
        # Since we are only interested in monodisperse droplets the outliers can
        # be removed. This reduces the error in the average diameter

        Dtemp = []
        I = []
```

```
    Iremove = []
    dropletID = []
    [dropletID.append(x) for x in df[’Droplet_ID’]  if x not in dropletID]
    for i in dropletID:
        droplet = df.loc[df[’Droplet_ID’] == i] # Extract only droplets with ID = i
        droplet = droplet.drop(droplet[droplet.X <= 200*10**(-6)].index) # remove droplets to the left of the middle (um)
        if len(droplet[’Frame’])>2:
            # Remove droplets with AR != 1
            # droplet = droplet.drop(droplet[droplet.AR < 0.98].index)
            # droplet = droplet.drop(droplet[droplet.AR > 1.02].index)
            Dtemp.append(s.mean(droplet[’D’]))
            I.append(i) # Droplet number
        else:
            Iremove.append(i) # Removes droplets with too few detections. Rarely happens.
            print(’\t\tError line’, inspect.currentframe().f_lineno, ’: Droplet with too few detections removed’)


    Davg_temp = s.mean(Dtemp) # Calculate mean of means. Only used as a threshold value

    ID = pd.DataFrame(zip(I, Dtemp), columns = [’I’, ’D’])
    ID = ID.drop(ID[ID.D < Davg_temp*1.01].index) # Ony keep instances where the diameter is above the average + 1% To be removed.
    Iremove+=ID[’I’].tolist() # Both droplets with few detection and too large will be removed
    for i in Iremove: # Remove droplets with too few datapoints and above average
        df = df.drop(df[df.Droplet_ID == i].index)

    """--------------------- Diameter --------------------------------------"""
    # Diameter is found by looking at relaxed droplets(to the right in the
    # frames for most exp). The AR must be close to 1 find spherical droplets.
    # all values are in micro meter.

    df_cut = df
    df_cut = df_cut.drop(df_cut[df_cut.AR < 0.98].index)
    df_cut = df_cut.drop(df_cut[df_cut.AR > 1.02].index)
    df_cut = df_cut.drop(df_cut[df_cut.X < 200*10**(-6)].index)
    D_avg = s.mean(df_cut[’D’])

    # Mean and standard deviation in m is added to lists.
    D.append(s.mean(df_cut[’D’]))
    DSD.append(s.stdev(df_cut[’D’]))

    """--------------------- Maximum deformation ---------------------------"""
    # The maximum deformation is found by finding the minimum value of AR for
    # each droplet an taking an average.

    minAR = []
    minXpos = []
    minH = []
    minW = []
    minFrame = []
    minDropletNr = []

    iterdrop = []
    [iterdrop.append(x) for x in df[’Droplet_ID’] if x not in iterdrop]
    for i in iterdrop: # Iterate trhough droplets IDs
        # Extract only droplets with ID = i
        droplet = df.loc[df[’Droplet_ID’] == i]
        minID = droplet.idxmin()  # Index at minimum, series
        loc = minID[’AR’] # Index, int
        # Add minimum value of AR and corresponsding x position to lists.
        minAR.append(droplet.loc[loc][’AR’])
        minXpos.append(droplet.loc[loc][’X’])


    AR.append(s.mean(minAR))   # Calculate average
    SD.append(s.stdev(minAR))     # Calculate SD
    xpos = s.mean(minXpos) # Average x position of deformation for velocity.

```

```
        """---------------------- Velocity ----------------------------------------"""
        # Velocity at maximum deformation is dertermined by calculating the
        # velocity of each droplet as the change in distance/change in time. A fit
        # is made and the value at the x position of maximum deformation is chosen.

        Udata = []
        Xdata = []
        iterdrop = []
        [iterdrop.append(x) for x in df[’Droplet_ID’] if x not in iterdrop]
        for i in iterdrop:
            # Extract only droplets with ID = i
            drop = df.loc[df[’Droplet_ID’] == i]
            diff = drop.diff()  # last row minus current row
            diff.dropna() # Remove NaNs
            # If difference in X is not negative and length is more than 0
            if (diff[’X’] < 0).values.any() == False and len(diff[’X’]) > 0:
                dist = diff[’X’].to_list()  # X difference from um to m
                sec = [f/8500 for f in diff[’Frame’]]  # Time from frame to seconds
                U = [c/t for c, t in zip(dist, sec)]   # Calculate Velocity m/s
                Udata.extend(U)                  # Add velocity to list
                Xdata.extend(drop[’X’].tolist())  # Add xpos to list
            else:
                print(’\t\tError line’, inspect.currentframe().f_lineno, ’: Velocity can not be calculated.’)


        udf = pd.DataFrame(list(zip(Xdata, Udata)), columns=[’X’, ’U’])
        udf = udf.dropna() # Remove NaNs (neccessary)
        x = udf[’X’].to_numpy()  # Make numpy arrays
        y = udf[’U’].to_numpy()  # Make numpy arrays

        # Initial guesses a, L, x0, k
        guess = [0.05, 0.3, 0.0002, 61000]
        parameters, pcov = curve_fit(
            sigmoid, x, y, p0=guess)  # Fit the curve

        # Velocity at x = min:
        V.append(
            sigmoid(xpos, parameters[0], parameters[1], parameters[2], parameters[3]))

        # Velocity error. Allow 5% on either side of xpos of max deformation.
        # Gives <10% deviation
        udf = udf.drop(udf[udf.X > xpos*1.05].index)
        udf = udf.drop(udf[udf.X < xpos*0.95].index)
        VSD.append(s.stdev(udf[’U’].tolist()))


        """---------------------- # of droplets ---------------------------------------"""
        # Return number of droplets detected
        iterdrop = []
        [iterdrop.append(x) for x in df[’Droplet_ID’] if x not in iterdrop]
        droplets.append(len(iterdrop))
        """---------------------- R* --------------------------------------"""
        # Calculate R*
        R.append(D[-1]/(100*10**-6)) #[m/m]

        """---------------------- Ca --------------------------------------"""
        # Calculate the capillary number
        Ca.append(eta*V[-1]/IFT) # Pa s *m/s / N/m = Nsmm/Nsmm = [-]

        """---------------------- Verification plots --------------------------------------"""
        fig, axes = plt.subplots(1, 5)
        plt.subplot(2, 2, 1)
        plt.scatter(df[’X’], df[’AR’], color=’navajowhite’)
        plt.plot([0, 0.0004], [AR[-1], AR[-1]], ’r’)
        plt.plot([0, 0.0004], [AR[-1]+SD[-1], AR[-1]+SD[-1]], ’:g’)
        plt.plot([0, 0.0004], [AR[-1]-SD[-1], AR[-1]-SD[-1]], ’:g’)
        plt.ylim(0.5, 1.2)
        plt.xlim(0.0001, 0.0003)
        plt.ticklabel_format(axis="x", style="sci", scilimits=(0,0))
        plt.ylabel(’AR’)
        plt.xlabel(’X-pos [m]’)
```

```

        plt.subplot(2, 2, 3)
        plt.scatter(df[’X’], df[’D’], color=’navajowhite’)
        plt.plot([0, 0.0004], [D[-1], D[-1]], ’r’)
        plt.plot([0, 0.0004], [D[-1]+DSD[-1], D[-1]+DSD[-1]], ’:g’)
        plt.plot([0, 0.0004], [D[-1]-DSD[-1], D[-1]-DSD[-1]], ’:g’)
        plt.ylim(6e-5, 1e-4)
        plt.xlim(0.0001, 0.0003)
        plt.ticklabel_format(axis="x", style="sci", scilimits=(0,0))
        plt.ylabel(’Diameter [m]’)
        plt.xlabel(’X-pos [m]’)

        plt.subplot(1, 2, 2)
        xspace = np.linspace(0, 0.0004, 100)
        velocity_plot = [sigmoid(
            x, parameters[0], parameters[1], parameters[2], parameters[3]) for x in xspace]
        plt.scatter(x, y, color=’navajowhite’)
        plt.plot(xspace, velocity_plot, ’r’)
        plt.plot([0, 0.0004], [V[-1], V[-1]], ’g:’)
        plt.plot([xpos, xpos], [0, 0.0004], ’:g’)
        plt.errorbar(xpos, V[-1], yerr=VSD[-1], xerr= xpos*0.05, capsize = 4, color = ’black’, marker = ’o’)
        plt.xlim(0.0001, 0.0003)
        plt.ticklabel_format(axis="x", style="sci", scilimits=(0,0))
        plt.ylabel(’V [m/s]’)
        plt.xlabel(’X-pos [m]’)
        name = d[result[-4]+1:result[-1]]
        plt.suptitle(name)
        fig.tight_layout()
        if save == ’y’:
            plt.savefig(path + r’\’’ + name+’_si.svg’, format = ’svg’)
        plt.show()

        t1 = time.time()
        total = t1-t0
        print(counter, ’/’, counter_tot, ’: ’, round(total, 1), ’seconds’)
        counter += 1


    print(’For-loop complete!’)
    data = pd.DataFrame(zip(conc, LP1, LP2, LP5, TotFlow, V, VSD, AR, SD, D, DSD, droplets, R, Ca), columns = [’conc’, ’LP1’, ’LP2’, ’LP5’, ’TotFlow’, ’Velocity’,’VDS’, ’AR’, ’SD’, ’D’, ’DSD’, ’droplets’, ’R*’, ’Ca’])

    if save == ’y’:
        savepath = path + r’\data_si.csv’
        data.to_csv(savepath, ’,’, index = False)
        print(’Data saved!’)
    end_time = time.time()
    print(’Total time: ’,round(end_time-start_time, 1), ’ seconds.’ )
print(’\nComplete!’)
```

NTNU
Norwegian University of
Science and Technology